Journal of Metamorphic Geology

WILEY

Journal of METAMORPHIC GEOLOGY

ORIGINAL ARTICLE OPEN ACCESS

Zircon Coupled Dissolution–Precipitation Replacement During Melt–Rock Interaction Modifies Chemical Signatures Resulting in Misleading Ages

Nathan R. Daczko[1] | Victoria Elliott[1] | Sandra Piazolo[2] | Kevin Hao[1]

[1]School of Natural Sciences, Macquarie University, Sydney, New South Wales, Australia | [2]School of Earth and Environment, University of Leeds, Leeds, UK

Correspondence: Nathan R. Daczko (nathan.daczko@mq.edu.au)

Received: 3 April 2024 | **Revised:** 30 July 2024 | **Accepted:** 15 September 2024

Funding: This study was financially supported by Australian Research Council Discovery Project (DP200100482) and internally through the School of Natural Sciences, Macquarie University.

ABSTRACT

Melt migration through Earth's crust drives well-documented melt–rock reactions, locally changing rock assemblage and geochemistry. However, melt–zircon interaction remains understudied. We report on three zircon-melt interaction events from the Pembroke Granulite, New Zealand. Primary zircon from gabbroic gneiss which was subject to minor post-emplacement melt migration and primary zircon from younger dykes exhibit straightforward microstructures, microchemistry, and age data. In contrast, zircon from melt-mediated reaction halos adjacent to the dykes and from melt-fluxed high-strain zones display dissolution modification of grains, micro-porosity and blurred or truncated internal zoning typical of replacement by coupled dissolution-precipitation. Replaced zircon domains show changed rare earth element patterns and redistributed or lost radiogenic Pb that generates ambiguous apparent spot date arrays, smeared over tens of millions of years. We conclude that the metamorphism and three melt–rock interaction events were brief, and the arrays misrepresent the true age and duration of the metamorphism. Pb-loss persisted beyond the metamorphism, with porosity and inclusions formed during coupled dissolution-precipitation making replaced zircon domains more susceptible to subsequent Pb-loss compared to the structurally intact, primary magmatic zircon in the host gabbroic gneiss or dykes. We recommend conducting high-resolution microstructural investigations upon recognition of spot date arrays observed in single samples to rule out the possibility of spurious arrays resulting from coupled dissolution-precipitation.

1 | Introduction

High-temperature U–Pb geochronometers, such as zircon ($ZrSiO_4$) and monazite ($(Ce,La,Nd,Th)(PO_4)$), are fundamental in determining the age and duration of magmatic and metamorphic events of the deep-time Earth system (e.g., Paces and Miller 1993; Vavra et al. 1996; Belousova et al. 2010; Yakymchuk and Brown 2014; Condie 2018). Furthermore, the substitution of useful geochemical tracer elements, such as Ti, Y, REE and Hf in zircon or Y, REE and U in monazite, enhances our understanding of tectonic settings, geological processes and reaction progression (Belousova et al. 2002, 2010; Cherniak and Watson 2007; Engi 2017; Rubatto 2017; Prent et al. 2019).

Issues arise when processes redistribute radiogenic Pb within grains and/or cause Pb-loss from grains, leading to the generation of misleading apparent spot dates. This phenomenon is demonstrated through both natural (Condit et al. 2018; Flowers, Schmitt, and Grove 2010; Halpin et al. 2020; Martin et al. 2008; Rubatto et al. 2008; Kunz, Regis, and Engi 2018;

Kusiak et al. 2013, 2019; Seydoux-Guillaume et al. 2015; Laurent et al. 2018; Skrzypek, Sakata, and Sorger 2020; Soman et al. 2010; Spier, Ferreira Filho, and Daczko 2022; Taylor, Kirkland, and Clark 2016; Tichomirowa, Whitehouse, and Nasdala 2005; Weinberg et al. 2020; Whitehouse, Ravindra Kumar, and Rimša 2014) and experimental studies (Grand'Homme et al. 2016; Varga et al. 2020; Asimus et al. 2024). While volume-diffusion is sluggish in crystalline zircon (Cherniak and Watson 2003; Möller et al. 2002) and monazite (Cherniak et al. 2004), various factors such as radiation damage (Mezger and Krogstad 1997), recrystallization (Piazolo, Austrheim, and Whitehouse 2012), fluid alteration (Geisler, Schaltegger, and Tomaschek 2007), crystal plastic deformation (Piazolo et al. 2016; Reddy et al. 2006, 2007; Timms, Kinny, and Reddy 2006) and coupled dissolution-precipitation (Geisler, Schaltegger, and Tomaschek 2007; Fougerouse et al. 2024) can induce the redistribution of Pb within a grain and cause Pb-loss from a grain. It should be noted that in geochronological studies, "recrystallization" of zircon has been associated with a process known as advection-diffusive interface-coupled dissolution–precipitation (Vonlanthen et al. 2012; Kelly et al. 2017; Poulaki et al. 2021; Bogdanova et al. 2021). This process involves zircon dissolution driven by fluid/melt, leading to the creation of embayments in the oscillatory-zoned cores. Subsequently, epitaxial mantles are formed through precipitation, and they grow while maintaining the crystallographic orientation of the zircon cores via interface-coupled precipitation (Vonlanthen et al. 2012). In the field of metamorphic studies, this specific process is commonly known as fluid-mediated interface-coupled replacement reactions, as discussed by Putnis (2009).

In contrast to the large number of studies focussing on deciphering the processes that may affect zircon apparent spot dates (e.g., Seydoux-Guillaume et al. 2015), detailed studies analysing the possible effect of such processes on geochemical tracer elements such as Hf or the rare earth elements are less common (see seminal studies by Gerdes and Zeh 2009; Martin et al. 2008). Hafnium is generally found to be decoupled from Pb-loss (e.g., Gerdes and Zeh 2009; Halpin et al. 2012), and changes to zircon trace element chemistry (e.g., Hf, Y, REE patterns and Th/U) are commonly linked to the growth environment and competition from nearby minerals (e.g., Möller et al. 2002; Rubatto 2017 and references therein).

In recent years, our understanding of the signature of fluid-mediated replacement reactions has increased significantly. For zircon, which is generally not affected by low temperature aqueous fluids, the most relevant fluid is a silicate melt. Melt-mediated coupled dissolution–precipitation replacement occurs in igneous systems, for example, where xenocrystic zircon interacts with host magmas (Miller et al. 2007; Paterson et al. 1992; Halpin et al. 2020; Spier, Ferreira Filho, and Daczko 2022) or in high-grade metamorphic systems where melt may react with zircon or monazite (Kohn et al. 2005; Kelsey, Clark, and Hand 2008; Yakymchuk and Brown 2014). Despite the occurrence of melt in a variety of igneous and high-T metamorphic systems, the impact of melt-mediated coupled dissolution-precipitation reactions on the geochronology and trace element signature of crucial U-bearing minerals like monazite and zircon remain poorly understood (e.g., Spier, Ferreira Filho, and Daczko 2022; Asimus et al. 2024).

To investigate in-depth the potential rare earth element and geochronological effect of melt–zircon interaction, we investigate zircon characteristics from well-studied granulites shown to have undergone at least three stages of melt–rock interaction (Stuart, Piazolo, and Daczko 2018b and references therein). Our investigation presents detailed microstructural observations, along with U–Pb-Hf isotope and trace element analyses, of zircon grains extracted from these granulites. Employing a combination of high-resolution imaging, alongside in situ trace element and isotopic analyses, we aim to establish connections between chemical variations in zircon and styles of melt–rock interaction, to better understand the age and duration of metamorphic processes. The primary goal is to enhance our comprehension of the processes responsible for redistributing radiogenic Pb, leading to the formation of near-concordant U–Pb spot date arrays that span tens of millions of years. We assess if these spot date arrays record geologically meaningful information.

Modified zircon grains in our natural case study exhibit irregular shapes, weak cathodoluminescence signals, silicate inclusions, low U concentrations, heightened discordance and varying REE contents. These data and observations suggest that melt-mediated coupled dissolution–precipitation replacement reactions significantly altered the microstructural and trace element characteristics of the zircon. This transformation has led to a broadening and smearing of the spot ages over approximately 20–25 million years, distinct from analytical scatter. Our results underscore the role of intragrain Pb redistribution and variable Pb-loss during (and following) melt-mediated coupled dissolution–precipitation in generating an intricate and heterogeneous distribution of U–Pb spot dates within melt–rock interaction scenarios.

1.1 | Regional Geology, Field Relationships and Details of Melt–Rock Interaction in the Pembroke Granulite

The gabbro protolith to the Pembroke Granulite was emplaced at 131.3 ± 2.9 Ma (Hollis et al. 2003), and this unit forms a low-strain component of the Arthur River Complex in New Zealand's South Island. It is a Cretaceous part of the Median Batholith, a composite, regional Cordilleran batholith emplaced into Palaeozoic crust in various pluses during Carboniferous to Early Cretaceous subduction along the paleo-Pacific margin of Gondwana (Mortimer et al. 1999). A pervasive S1 foliation, defined by enstatite, diopside, brown-green pargasite, plagioclase and ilmenite, is observed in the granulite, exhibiting variations from magmatic to partially recrystallised in gabbroic gneiss (Figures 1a and 2a,b; Blattner 1976, 2005; Daczko, Clarke, and Klepeis 2001a; Stuart, Piazolo, and Daczko 2016).

Deformation and metamorphism, involving three main types of melt–rock interaction, overprint the gabbroic gneiss (Table 1). Type I melt–rock interaction represents diffuse porous melt flow which heterogeneously permeated the grain boundary network; melt ingress and migration through the gneiss were facilitated by minor in situ partial melting resulting in local grain boundary melt networks (Stuart, Piazolo, and Daczko 2016). Type I melt–rock interaction was intertectonic (static) and is characterised by hydration reactions where coronas of blue-green pargasite

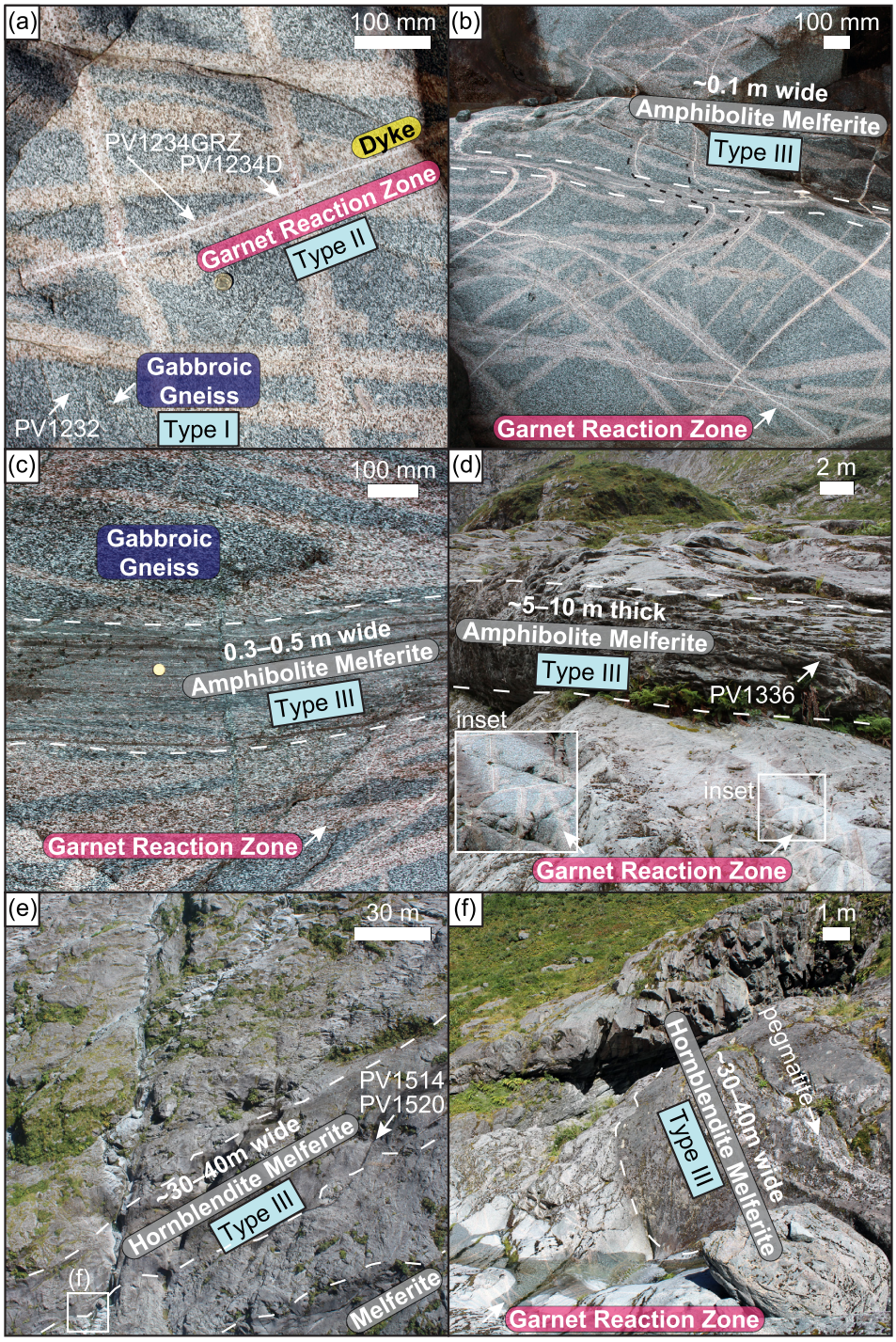

FIGURE 1 | Pembroke Granulite field relationships linked to three types of melt–rock interaction. (a) Gabbroic gneiss with S1 gneissosity was modified by Type I static diffuse porous melt flow which heterogeneously permeated the grain boundary network and weakly hydrated the gneiss (grey rock, representative sample PV1232). The gabbroic gneiss is cut by a rectilinear pattern of trondhjemitic dykes (white rock, representative sample PV1234D) with adjacent garnet reaction zones (pink rock, representative sample PV1234GRZ) that formed by Type II melt–rock interaction. Rock types in panel (a) are cut by melferite high-strain zones comprising: (b, c) narrow (< 0.5 m wide), steeply dipping amphibolite melferite, (d) metre-thick shallowly dipping amphibolite melferite (representative sample PV1336), and (e, f) decimetre-wide hornblendite melferite (representative samples PV1514 and PV1520).

and quartz partially replaced pyroxene grains (Figure 2a), at $T = 630°C–710°C$ and $p = 8.8–12.4$ kbar (Stuart, Piazolo, and Daczko 2016). The time-integrated melt flux was low (Stuart, Piazolo, and Daczko 2018b), and the modification of the gneiss was minor (representative sample PV1232).

Type II melt–rock interaction (Table 1) took place during a significant regional magmatic flare-up event (126–115 Ma), characterised by the emplacement of high Sr/Y magma into the arc system (Allibone et al. 2009; Milan et al. 2016; Milan, Daczko, and Clarke 2017; Tulloch and Kimbrough 2003).

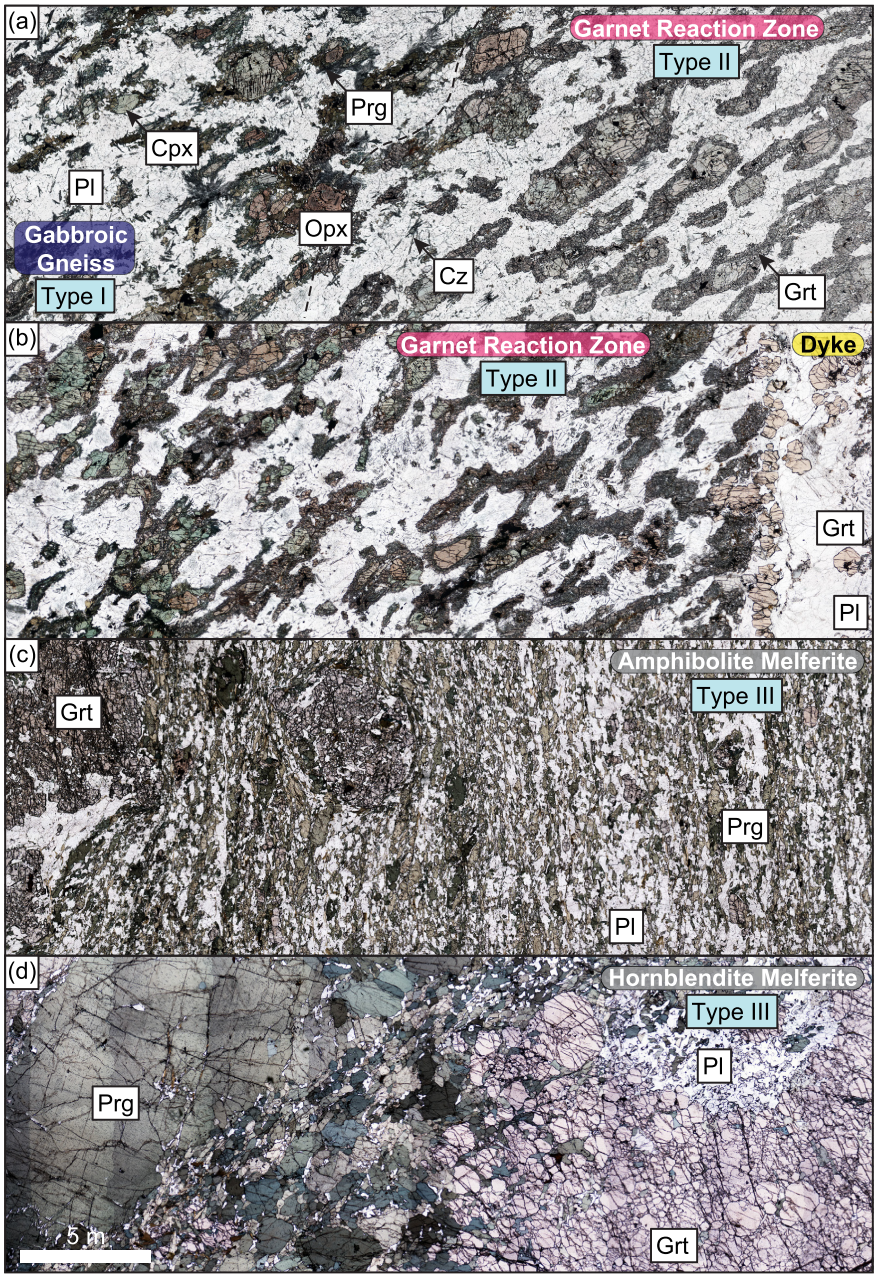

FIGURE 2 | Petrographic overview of the key rock types. (a) Gabbroic gneiss (left of black dashed line) with S1 foliation, defined by enstatite orthopyroxene (Opx), diopside clinopyroxene (Cpx), brown-green pargasite (Prg), plagioclase (Pl) and ilmenite (opaque). Note hydration during Type I melt–rock interaction formed asymmetric pargasite-rich coronae around the pyroxene grains and clinozoisite (Cz) in plagioclase. Garnet reaction zones (right of black dashed line in panel (a) and adjacent to the dyke in panel (b)) formed during Type II melt–rock interaction and show the melt-mediated dehydration of pargasite to form coronae of garnet (Grt) and diopside around relict S1 pyroxene grains. The mode of garnet increases towards the garnet-plagioclase trondhjemitic dykes (b). (c) Amphibolite melferite, formed during moderate to high time-integrated melt flux and extensive melt–rock interaction (Type III), displays a new foliation that is predominantly defined by pargasite and plagioclase. Coarse syn-tectonic peritectic garnet grains occur in some amphibolite melferite samples (Stuart et al. 2018a). (d) Hornblendite melferite is dominated by pargasite with very minor interstitial plagioclase that has completely replaced the precursor gabbroic gneiss. Garnetite stringers have replaced garnet reaction zones (see Daczko et al. 2016 and Meek, Piazolo, and Daczko 2019 for more details).

Locally, numerous subvertical, narrow, garnet-bearing, trondhjemitic D2 dykes (representative sample PV1234D) intruded the two-pyroxene-pargasite granulite in a rectilinear pattern (Figure 1a,b; Blattner 1976, 2005; Daczko, Clarke, and Klepeis 2001a). A garnet Sm-Nd age of 122.6 ± 2.0 Ma dates this event (Stowell et al. 2010). Type II melt–rock interaction occurred adjacent to the D2 dykes forming garnet reaction zones (GRZ) within < 80-mm-wide high-P, melt-mediated, dehydration reaction haloes (representative sample PV1234GRZ, sampled directly adjacent to PV1234D; Figure 1a,b). Garnet-diopside assemblages statically replace the pargasite coronae around pyroxene grains, pseudomorphing the S1 gneissosity

TABLE 1 | Characteristics of melt–rock interaction styles of the Pembroke Granulite and associated samples.

Melt–rock interaction event types	(I) Intertectonic minor diffuse porous flow	(II) Dyke-related garnet reaction zone	(III) High melt flux melferite
Process	Distributed melt migration along grain boundaries via diffuse porous flow, static conditions	Local melt-mediated reaction halo adjacent to dykes, static conditions	Deformation-assisted diffuse porous melt flow in actively deforming high-strain melferite zones, syntectonic, dynamic conditions
Melt flux style of Stuart, Piazolo, and Daczko (2018b)	1	—	3–4
Timing	Intertectonic (between D1 and D2); after Zrc U–Pb c. 131 Ma emplacement age (Hollis et al. 2003, this study) and before D2	D2; Grt Sm-Nd = 122.6 ± 2.0 Ma (Stowell et al. 2010); Zrc U–Pb = 123.5 ± 1.5 Ma (this study)	D3; Grt Sm-Nd = 126.0 ± 2.1 Ma (Stowell et al. 2010)
Degree of metasomatism, changes in activity of water	Limited to no metasomatism, e.g., local Sr increase in plagioclase, hydration, melt pseudomorphed by Pl, Kfs, Qtz, Prg	Limited metasomatism, e.g., minor Na loss and Cu gain, dehydration	Minor to significant metasomatism, e.g., LREE gain and HREE loss, hydration, melt pseudomorphed by Pl, Kfs, Qtz, Pg, Cz, Bt, Grt
Characteristics of melt	Minor in situ partial melting and limited fluxing by externally derived hydrous mafic melt	Dyking by externally derived anhydrous trondhjemitic melt and local melt-mediated reaction halo	Minor in situ partial melting and moderate to extensive fluxing by externally derived hydrous mafic melt
Time-integrated melt flux and relative modification of protolith(s)	Low (limited coronae of Pg-Qtz around Px, high retainment of original minerals)	Moderate flux via dyking, low flux into the reaction halo where modification is high (partial replacement of 2-Px-Pg granulite with Grt granulite reaction zones, retainment of some original minerals)	High to very high (complete replacement of 2-Px-Pg granulite, dykes and GRZ with amphibolite and hornblendite melferite)
Representative samples (Figure 1)	Gabbroic gneiss (PV1232)	Dyke (PV1234D), Garnet reaction zone (PV1234GRZ)	Amphibolite melferite (PV1336), hornblendite melferite (PV1514, PV1520)
Literature	Stuart, Piazolo, and Daczko 2016	Blattner 1976, 2005 Daczko, Clarke, and Klepeis 2001a Smith et al. 2015	Daczko et al. 2016 Stuart et al. 2018a; Stuart, Piazolo, and Daczko 2018b Meek, Piazolo, and Daczko 2019
Zircon crystallisation and modification (as determined in this study)	Pre-existing c. 131 Ma primary magmatic zircon (± minor xenocrysts) in gabbro is not modified during this Type I melt–rock interaction event	New c. 124 Ma primary magmatic zircon crystallisation in dykes; extensive modification of pre-existing c. 131 Ma zircon in garnet reaction zones; some younger Pb-loss demonstrated	No new zircon crystallisation in melferite zones; extensive modification of pre-existing c. 131 Ma and c. 124 Ma zircon; impregnation of zircon xenocrysts carried by fluxing melt; some younger Pb loss likely

(Figure 2a,b). Thermobarometry of the garnet reaction zones indicates peak metamorphic conditions of 680°C–815°C and 11–14 kbar (Clarke, Klepeis, and Daczko 2000; Daczko and Halpin 2009; Stowell et al. 2010). Although melt flux through the dykes may have been high, limited chemical change is identified by comparing the host gabbroic gneiss to the garnet reaction zone and suggests that melt ingress from the dyke into the gabbroic gneiss was limited (Daczko, Clarke, and Klepeis 2001a). This indicates low time-integrated melt flux for type II melt–rock interaction within the garnet reaction zones.

The magmatic flare-up event was also concurrent with magmatic and tectonic thickening of the arc root (Allibone

et al. 2009). During this period, D3 contractional deformation of the Pembroke Granulite formed shallowly and steeply dipping high-strain zones (Figure 1b–f; Daczko, Klepeis, and Clarke 2001b). D3 deformation was localised, preserving the low-strain domains of lower crustal assemblages described above. S3 is defined by peritectic garnet, magnesio-hornblende, clinozoisite, plagioclase and biotite, in well foliated and lineated rocks (Figures 1d and 2c), and D3 occurred at $T = 675°C$ and $p = 14$ kbar (Daczko, Klepeis, and Clarke 2001b), involving minor partial melting within the high-strain zones (Stuart, Daczko, and Piazolo 2017).

Type III melt–rock interaction (Table 1) is associated with largely externally sourced hydrous melt that migrated 'up' D3 ductile shear zones during the deformation, forming melferite (Daczko and Piazolo 2022), i.e., rocks formed by melt–rock interaction in high-strain melt migration pathways (Figure 1b–f). The interactions drove complete replacement and hydration of the D1 two-pyroxene-pargasite and D2 dykes and garnet-diopside granulite reaction zones to variably form melferite zones comprising (1) garnet-bearing amphibolite (representative sample PV1336; Figures 1b–d and 2c; Daczko, Klepeis, and Clarke 2001b; Stuart et al. 2018a) and (2) garnet-bearing hornblendite (representative samples PV1514 and PV1520; Figures 1e,f and 2d; Daczko et al. 2016; Stuart, Piazolo, and Daczko 2018b; Meek, Piazolo, and Daczko 2019). The time-integrated melt flux and the modification of precursor rocks were moderate to high (Stuart, Piazolo, and Daczko 2018b) in the melferite zones.

The timing of the Type III melt–rock interaction event is dated by garnet Sm-Nd analysis from a sample of garnet-bearing hornblendite (126.0 ± 2.1 Ma, Stowell et al. 2010). The overlapping garnet Sm-Nd geochronology for both Types II and III melt–rock interaction events indicates short-lived events that occurred within 5–10 million years after emplacement of the host gabbro (131.3 ± 2.9 Ma; Hollis et al. 2003). Dating of apatite (U–Pb) and hornblende, mica and plagioclase (Ar-Ar) shows that decompression and exhumation occurred within 20 Myr of peak metamorphism (see compilation of Daczko, Clarke, and Klepeis 2002) and involved little retrogressive overprint, preserving lower crustal assemblages. Exceptional exposure in the Pembroke Valley, due to recent deglaciation, affords a valuable site for studying melt transfer zones in the lower crust of magmatic arcs and the impact of melt–rock interaction on zircon geochronology.

2 | Sampling and Methods

2.1 | Legacy Samples and Mineral Separation

Representative Pembroke Granulite legacy samples showcasing three melt–rock interaction styles (Table 1) were processed for zircon separation at Macquarie University. Petrographic descriptions and characterisation of these rock types are available in Clarke, Klepeis, and Daczko (2000), Clarke et al. (2005), Daczko, Clarke, and Klepeis (2001a), Daczko, Klepeis, and Clarke (2001b), Daczko et al. (2016), Schröter et al. (2004), Smith et al. (2015), Stuart, Piazolo, and Daczko (2016, 2018b), Stuart, Daczko, and Piazolo (2017), Stuart et al. (2018a), Meek, Piazolo, and Daczko (2019), and Daczko and Piazolo (2022). A high-resolution image of the thin sections and other associated data can be examined online at ImageMatrix: https://imagematrix.science.mq.edu.au, search using PV < sample# >, e.g., PV1234.

Tungsten-carbide mills were used to disaggregate four rock samples (dyke: PV1234D, garnet reaction zone: PV1234GRZ, amphibolite melferite: PV1336, hornblendite melferite: PV1514), while high-voltage electric pulsed SelFrag rock disaggregation was utilised for gabbroic gneiss (PV1232) and a second sample of hornblendite melferite (PV1520). After disaggregation, samples were sieved into fractions: > 600, 300–600 and < 300 μm. The < 300-μm fraction underwent panning to concentrate heavy minerals, followed by standard magnetic and heavy liquid mineral separation procedures. Zircon grains were hand-picked from the final concentrate under a binocular microscope, aided by a UV lamp, mounted in epoxy and polished to expose the midsections.

2.2 | Zircon Analysis

2.2.1 | Imaging of Zircon Morphology and Internal Structures

Standard backscattered electron (BSE) and cathodoluminescence (CL) images were taken to characterise the morphology and internal structure of all separated zircon grains using a Zeiss EVO MA15 scanning electron microscope at Macquarie University. Additional high-resolution BSE images were taken using a FEI Teneo field emission scanning electron microscope at Macquarie University. All backscattered electron and cathodoluminescence images of zircon can be examined online at ImageMatrix (e.g., search for PV1232). Representative grains are shown in Figures 3 and 4. These images were used for distinguishing primary growth features from potentially modified grains. Optimal locations for laser ablation inductively coupled plasma mass spectrometry (LA-ICP-MS) and laser-ablation multicollector inductively coupled plasma mass spectrometry (LA-[MC]-ICP-MS) were chosen based on backscattered electron and cathodoluminescence characterisation.

2.2.2 | U–Pb Geochronology

In situ U–Pb dating was conducted on zircon grains using the Photon Machines Excimer laser-ablation system with a beam wavelength of 193 nm, coupled with an Agilent 7700 series quadrupole ICP-MS at Macquarie University. Following the methods of Jackson et al. (2004), U–Pb dating was performed separately from trace element analysis for higher precision. Isotopes measured included ^{204}Pb, ^{206}Pb, ^{207}Pb, ^{208}Pb, ^{232}Th and ^{238}U. Reference zircon GJ-1 (Horstwood et al. 2016) was analysed at the beginning and end of each run for instrument calibration. GLITTER software facilitated data reduction and signal selection. Weighted mean $^{206}Pb/^{238}U$ ages for the secondary zircon standards 91,500 and Mud Tank over the course of this study (at 95% confidence) are 1061 ± 6 Ma ($n = 5/10$, MSWD = 2.7) and 729 ± 3 Ma ($n = 10/10$, MSWD = 0.03),

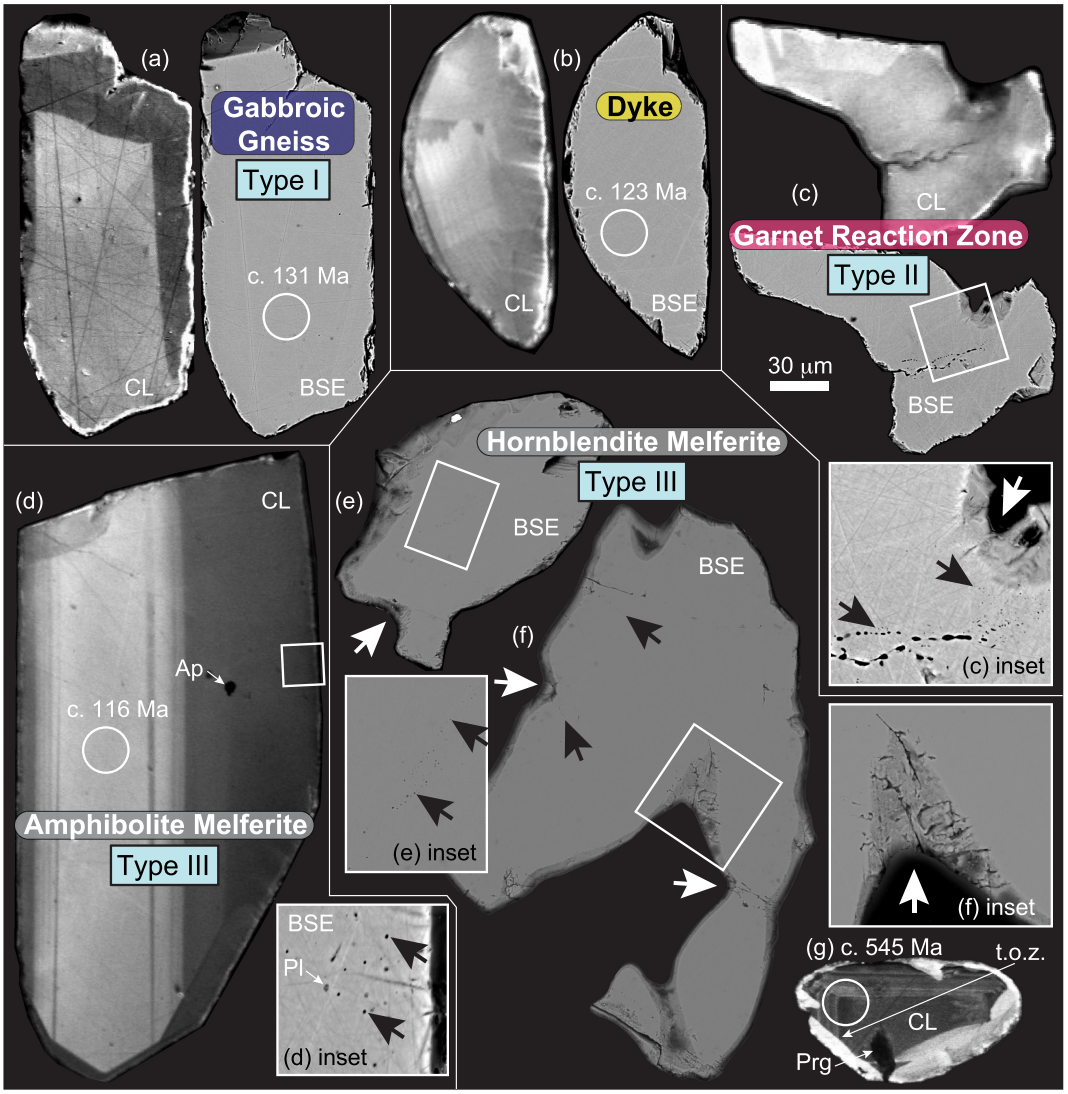

FIGURE 3 | Microstructural characterisation of representative zircon in cathodoluminescence (CL) and backscattered electron (BSE) images. (a) gabbroic gneiss zircon (PV1232), (b) trondhjemitic dyke zircon (PV1234D), (c) garnet reaction zone zircon (PV1234GRZ), (d) amphibolite melferite zircon (PV1336), (e–g) hornblendite melferite zircon (PV1514 and PV1520). Key microstructures include dissolution embayments of grain boundaries with pitted surfaces (white arrows), porosity trails and dissolution channels (black arrows), mineral inclusions (labelled) and blurred to truncated cathodoluminescence responses. t.o.z = truncated oscillatory zoning.

compared to the published CA-ID-TIMS zircon ages of 1063.5 ± 0.8 Ma and 731.65 ± 0.98 Ma (Horstwood et al. 2016), respectively. The primary zircon standard GJ-1 yields a $^{206}Pb/^{238}U$ weighted mean age of 600.9 ± 1.2 Ma (n = 38/38, MSWD = 0.24) within uncertainty of the recommended value of 601.86 ± 0.74 Ma (Horstwood et al. 2016). Data from our samples and method metadata are provided in Table S1a,b.

2.2.3 | Trace Element Analysis

In situ trace element analysis was conducted on a separate spot on zircon grains for elements Si, P, Ti, Y, Zr, Nb, La, Ce, Pr, Nd, Sm, Eu, Gd, Dy, Ho, Er, Yb, Lu, Hf, Ta, Pb, Th and U, using the Photon Machines Excimer laser-ablation system with a beam wavelength of 193 nm, coupled with an Agilent 7700 series quadrupole ICP-MS at Macquarie University. Reference standard glass NIST 610 was used as the external calibration standard. The GLITTER software package was employed for signal selection, and trace element concentrations were calibrated using stoichiometric Zr content in zircon of 48.5 wt.%. Data from our samples and method metadata are provided in Table S1c,d. Data for the secondary glass standard (BCR-2; Jochum et al. 2007) and secondary zircon standard (GJ-1; Exertier et al. 2018) match the recommended values (Table S1c).

2.2.4 | Lu-Hf Analysis

In situ Hf isotopic analysis was performed on separate spots on zircon grains using a New Wave Research laser-ablation microprobe (213 nm) coupled with a Nu Plasma (MC) ICP-MS at Macquarie University. Ablation locations were chosen

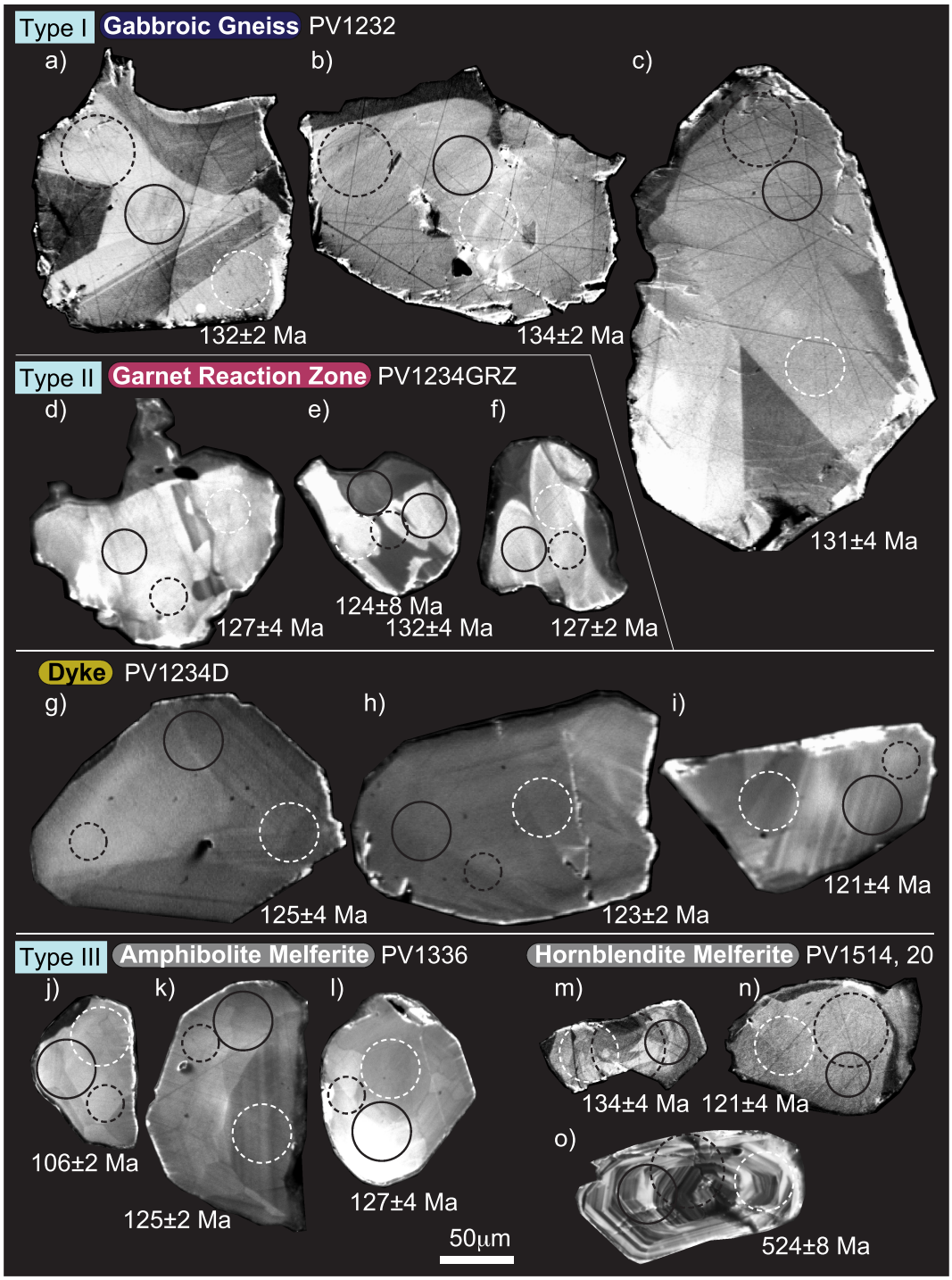

FIGURE 4 | Spot analysis locations on representative zircon in cathodoluminescence (CL) images. (a–c) gabbroic gneiss zircon (PV1232), (d–f) garnet reaction zone zircon (PV1234GRZ), (g–i) trondhjemitic dyke zircon (PV1234D), (j–l) amphibolite melferite zircon (PV1336), (m–o) hornblendite melferite zircon (PV1514 and PV1520). Analysis positions are black circle (U–Pb), white dashed circle (trace elements) and black dashed circle (Hf isotopes).

close to U–Pb and trace element analysis pits within the same region of BSE-CL intensity/type. Minimum model ages (TDM) were calculated based on a depleted-mantle source using Griffin et al. (2004) model parameters. Crustal model age (TcDM) was determined using the measured $^{176}Lu/^{177}Hf$ ratio and decay constant as described by Scherer, Munker, and Mezger (2001). εHf values were calculated as per Scherer, Munker, and Mezger (2001). Data from our samples and method metadata are provided in Table S1e,f. Data for the Mud Tank and Temora-2 reference zircon standards were collected during our study average $^{176}Lu/^{177}Hf = 0.282526 \pm 73$ (2SD) and $^{176}Lu/^{177}Hf = 0.282676 \pm 38$ (2SD; Table S1e), respectively. These values are within uncertainty of the recommended values for Mud Tank (0.282523 ± 10 (2SD); e.g., Gain et al. 2019) and Temora-2 (0.282680 ± 31 (2SD); e.g., Wu et al. 2006).

3 | Results

3.1 | Zircon Microstructure

The separated zircon grains from all rock samples are typically elongate and irregular in shape with faint cathodoluminescence responses. Grains from the gabbroic gneiss (PV1232, 100–300 μm) and dyke (PV1234D, 150–250 μm) display subhedral to anhedral grain shapes (Figure 3a,b, Figure 4a–c, g–i), with rare crystal facets and pyramidal terminations being more common in the dyke sample (Figures 3b and 4g–i). Internal cathodoluminescence response is low, varying between homogeneous and sector-, planar- or oscillatory-zoned internal character (Figures 3a,b and 4a–c, g–i). Oscillatory zoning in zircon is more common (70% of grains) in the dyke sample (Figures 3b and 4g–i).

In contrast, zircon grains from the garnet reaction zone sample (PV1234GRZ, 50–150 μm; Type II melt–rock interaction) and the melferite samples (PV1336B, PV1514, PV1520, 50–150 μm; Type III melt–rock interaction) are generally smaller. However, rare larger grains (up to 350 μm) are distinctly euhedral (Figure 3d) or highly irregular and embayed (white arrows, Figure 3f). The embayed areas show well developed dissolution pitting of the zircon surface (Figure 3f inset). Cathodoluminescence response is generally higher for grains from the garnet reaction zone (Figures 3c and 4d–f) compared to the melferite samples (Figures 3d,g and 4j–o). Most zircon grains display homogeneous or sector zoning; some grains have patchy irregular bright- and dark-cathodoluminescence response, particularly in the garnet reaction zone zircon grains (Figures 3c and 4d–f). However, very rare grains in the melferite samples display banded zoning (Figure 3d) or well-developed oscillatory zoning that is truncated by thin brightly luminescent rim domains (Figures 3g and 4o). Many zircon grains from the garnet reaction zone and melferite samples contain very small (< 1–3 μm) circular to irregular pores and highly elongate and variably thick discontinuous channels (Figure 3c–f insets). Pores may occur in domains within grains (Figure 3e), particularly near the embayed grain boundaries (Figure 3f inset) or form discontinuous trails of variable length (black arrows, Figure 3f). Mineral inclusions are rare in the garnet reaction zone zircon grains but common in the melferite zircon which contain pargasite, plagioclase feldspar, rutile and apatite within some pores and channels (Figure 3d).

3.2 | Zircon Trace Elements

Trace element analytical spot locations were guided by our microstructural characterisation of the zircon (Section 3.1). Indistinguishable steep, chondrite-normalised rare earth element patterns, with positive Ce and negative Eu anomalies (Figure 5a) characterise zircon from the gabbroic gneiss and garnet reaction zone samples (blue lines and pink lines, respectively, Figure 5a), which experienced Types I and II melt–rock interaction, respectively. The garnet reaction zone zircon is slightly lower in heavy rare earth elements on average compared to the gabbroic gneiss zircon (Figure 5a), although the degree of depletion has low correlation with the spot date of each grain (Table S1c,g). Y concentrations in zircon are uniformly high in these two samples but are scattered to lower contents for the garnet reaction zone zircon (Figure 5d; Y = 333–1411 ppm for gabbroic gneiss and 190–673 ppm for zircon in garnet reaction zones). Y is well-correlated with Eu in gabbroic gneiss zircon (Figure 5d). Hf content is relatively constant and has moderate values of 1.05–1.20 wt.% HfO_2 in zircon from gabbroic gneiss and spreads to lower contents of 0.97–1.17 wt.% HfO_2 in zircon from garnet reaction zones (compare blue filled versus pink circles, Figure 5e). U and Th concentrations are typically low to moderate, ranging from tens of ppm to ~200 ppm (Table S1a). Th/U ratios are consistently high (0.66–1.06 for gabbroic gneiss and 0.40–1.46 for garnet reaction zones; Table S1a).

Zircon from the trondhjemitic D2 dykes have different trace element characteristics compared to the gabbroic gneiss and garnet reaction zone samples. These are lower in heavy rare earth elements and lack the pronounced Eu anomaly, showing an overall flatter rare earth element pattern (yellow fill, Figure 5b). Y contents are considerably lower (Figure 5d, 51–311 ppm) than gabbroic gneiss and garnet reaction zone samples, whereas the concentrations of Hf (Figure 5e), U and Th are similar (0.93–1.30 wt.% HfO_2, tens to ~200 ppm U and Th; Table S1a). Th/U ratios are lower (0.30–0.74; Table S1a).

Zircon from the melferite samples (Type III melt–rock interaction) fall into three groups of trace element patterns. Most zircon grains (Group 1: $n = 15$ from the amphibolite melferite and $n = 3$ from the hornblendite melferite) have different trace element characteristics compared to the gabbroic gneiss, garnet reaction zone and dyke zircon grains (light grey fill, Figure 5c). These have even lower heavy rare earth element contents than the dyke, showing the flattest rare earth element patterns of all our data (Figure 5c). Y contents are the lowest in these Group 1 melferite (39–191 ppm) zircon, whereas the concentrations of Hf, U and Th are more variable (0.81–1.78 wt.% HfO_2, tens to > 900 ppm U and Th; Table S1a). Th/U ratios show the lowest range of all samples (0.37–0.58; Table S1a).

A second group of zircon grains from the melferite samples comprises six grains ($n = 1$ from the amphibolite melferite and $n = 5$ from the hornblendite melferite) that have rare earth element patterns (green lines, Figure 5c) and HfO_2 contents (0.89–1.28; Table S1c) that largely overlap those from the gabbroic gneiss and garnet reaction zones. However, Y, Eu, U and Th concentrations in these six zircon grains are highly variable (Figure 5d; Y = 305–1920 ppm; Y = 0.11–2.46 ppm; U = 56–1192 ppm; Th = 36–475 ppm). Th/U ratios are moderate (0.25–0.63; Table S1a).

The third group of zircon grains from the melferite samples comprises five grains (all from hornblendite melferite) that have very low light rare earth element contents (orange lines, Figure 5c). Y concentrations in these five zircon grains are highly variable (Figure 5d; 15–1717 ppm), whereas these have similar HfO_2 contents (0.80–1.24) to zircon from other rocks (Figure 5e). U and Th concentrations and Th/U ratios are extremely low, (< 3 ppm U, < 0.25 ppm Th, Th/U = 0.004–0.14; in some case below detection limits; Table S1a).

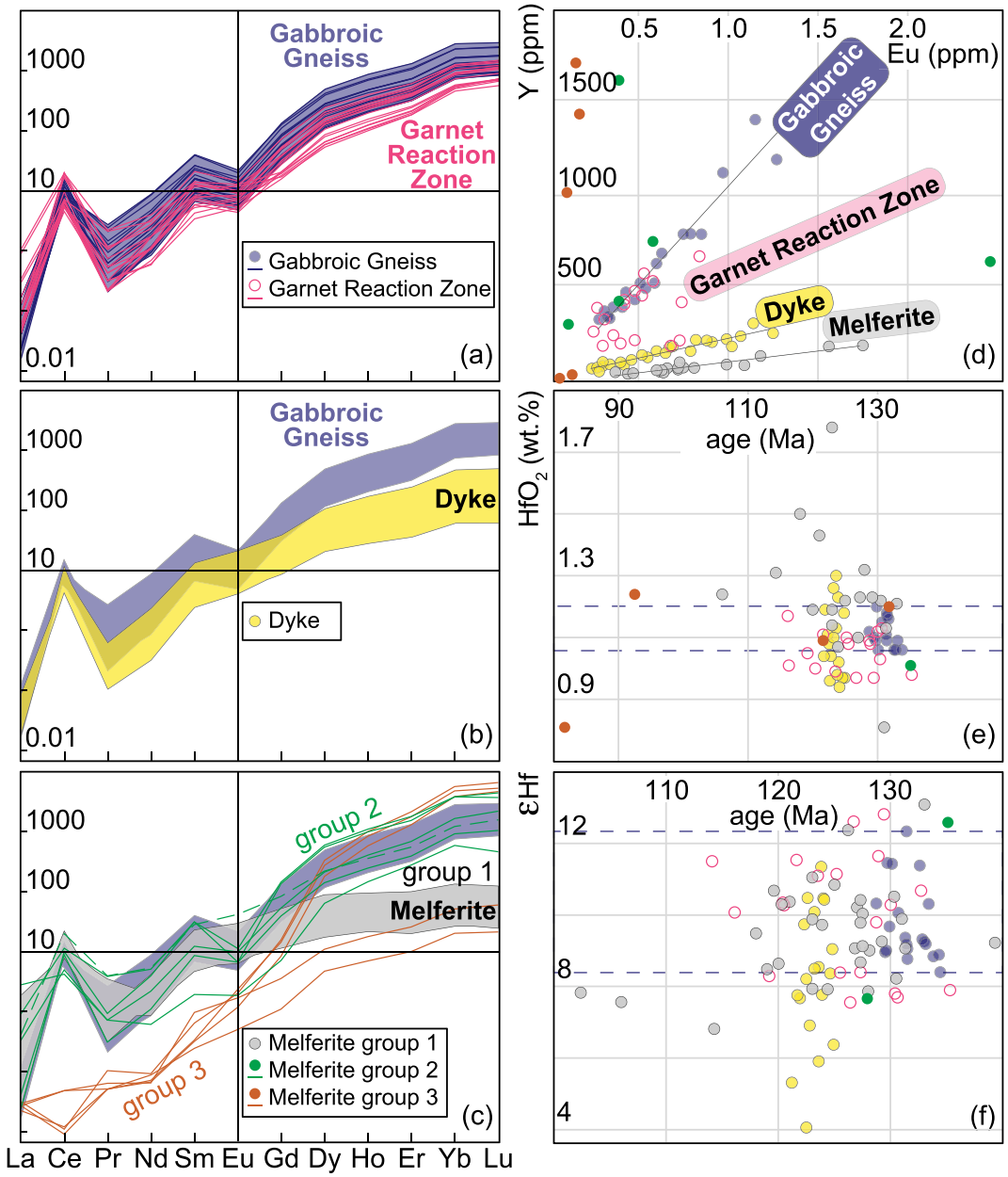

FIGURE 5 | Geochemical characterisation of zircon. All data and uncertainties are reported in Table S1c. (a–c) Chondrite normalised (Sun and McDonough 1989) zircon rare earth element patterns for (a) gabbroic gneiss (Type I melt–rock interaction, PV1232) and garnet reaction zone (Type II melt–rock interaction, PV1234GRZ), (b) dyke (PV1234D), and (c) melferite samples (Type III melt–rock interaction with three geochemical groups: Group 1 = grey-filled area; Group 2 = green lines; Group 3 = orange lines; see text for more details, PV1336, PV1514 and PV1520). (d–f) Bivariate plots of (d) Yttrium (Y) versus Europium (Eu), (e) HfO_2 versus apparent spot date and (f) epsilon Hf versus apparent spot date.

3.3 | Zircon U–Pb Geochronology and Hf-Isotope Character

Twenty-one signal selections were made from 21 spot analyses of the zircon separated from the gabbroic gneiss (PV1232, Type I melt–rock interaction). The $^{206}Pb/^{238}U$ spot dates range between 129 ± 2 and 134 ± 5 Ma. The $^{206}Pb/^{238}U$ weighted mean age is 131.4 ± 1.2 Ma (n = 21, MSWD = 1.3, p(χ2) = 0.14) (Figure 6a,c).

Twenty-one signal selections were made from 21 spot analyses of the zircon separated from the dyke (PV1234D). The $^{206}Pb/^{238}U$ spot dates range between 121 ± 4 Ma and 125 ± 5 Ma. The $^{206}Pb/^{238}U$ weighted mean age is 123.5 ± 1.5 Ma (n = 21, MSWD = 0.34, p(χ2) = 1) (Figure 6a,c).

Twenty-six signal selections were made from 26 spot analyses of the zircon separated from the garnet reaction zone sample (PV1234GRZ, Type II melt–rock interaction). While most spot dates are better than 95% concordant, two spot dates are greater than 10% discordant (Figure 6d,f). The concordant $^{206}Pb/^{238}U$ spot dates range between 114 ± 3 Ma and 135 ± 3 Ma (Figure 6d), with one outlier concordant spot date at 172 ± 8 (Figure 6f). A statistically valid $^{206}Pb/^{238}U$ weighted mean age could not be determined due to scatter in the population (Figure 6d).

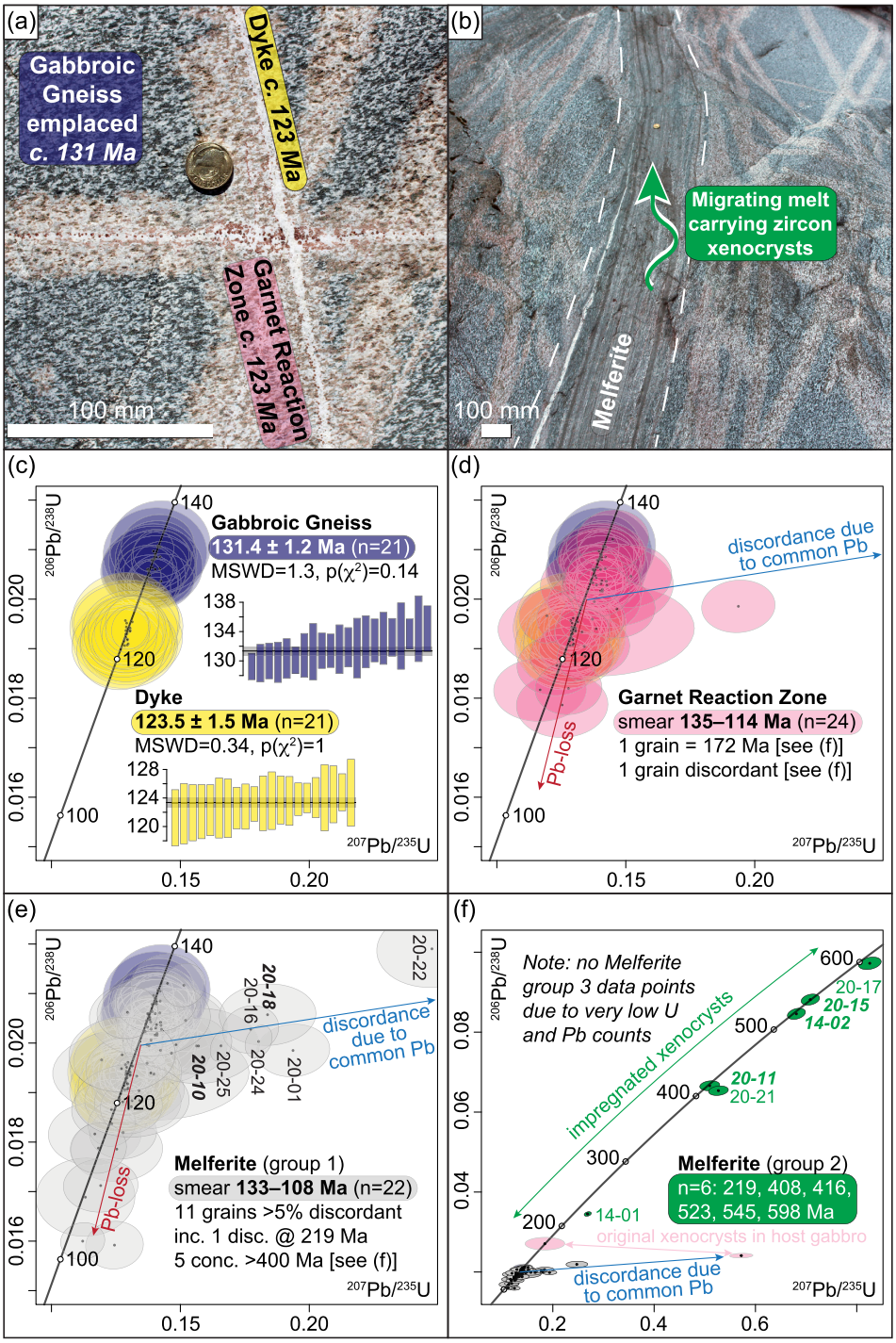

FIGURE 6 | Zircon geochronology. (a–b) Field relationship context for the colour scheme used on the graph panels (same colour scheme as Figure 5). (c–f) Wetherill and $^{206}Pb/^{238}U$ weighted mean age plots of zircon produced using IsoplotR (Vermeesch 2018). See text for interpretations.

The zircon signature of Type III melt–rock interaction from melferite samples is highly diverse and we divide these into the three trace element groups determined in section 3.2. Twenty-seven signal selections were made from 27 spot analyses of the zircon separated from the melferite samples that have the HREE-depleted (Group 1) rare earth element patterns (grey-filled, Figure 5c; amphibolite melferite PV1336B [$n=13$], two samples of hornblendite melferite PV1514 [$n=1$] and PV1520 [$n=13$]). While 15 of the spot dates are better than 95% concordant, six spot dates are greater than 10% discordant (the most discordant grain numbers are labelled on Figure 6e). The 15 concordant $^{206}Pb/^{238}U$ spot dates range between 114 ± 3 and 133 ± 3 Ma, with two outlier concordant spot dates of 408 ± 6 and 598 ± 7 Ma. A statistically valid $^{206}Pb/^{238}U$ weighted mean age could not be determined due to scatter in the population (Figure 6e).

Six signal selections were made from six spot analyses of the zircon separated from the melferite samples that have the HREE-enriched (Group 2) rare earth element patterns (green

lines, Figure 5c; all from the two samples of hornblendite melferite PV1514 [$n=1$] and PV1520 [$n=4$]). Three of the spot dates are better than 95% concordant, and three spot dates are greater than 5% discordant (the grain numbers are labelled on Figure 6f). The three concordant $^{206}Pb/^{238}U$ spot dates are 416 ± 6, 523 ± 7 and 545 ± 7 Ma, while the three discordant spot dates hint at Neoproterozoic and Mesozoic dates. A statistically valid $^{206}Pb/^{238}U$ weighted mean age could not be determined due to scatter in the population (Figure 6e).

Ten signal selections were made from 10 spot analyses of the zircon separated from the melferite samples that have the LREE-depleted (Group 3) rare earth element patterns (orange lines, Figure 5c; all from the hornblendite melferite PV1520 [$n=10$]). All 10 of the spot dates are highly discordant, and the date determined is unreliable due to very low counts of U and Pb isotopes (Table S1a) and none of the data from Group 3 are plotted on Figure 6f.

The Hf isotopic character of zircon (Figure 5f and Table S1) is highly radiogenic and comparable from the gabbroic gneiss (Figure 5f; $\varepsilon Hf = +8.40$ to $+12.33$) and garnet reaction zone (Figure 5f; $\varepsilon Hf = +7.55$ to $+12.81$) samples. However, over one-quarter of analyses from the garnet reaction zone are less radiogenic (Figure 5f; 6/22 grains with $\varepsilon Hf = +7.55$ to $+8.39$) than zircon in the gabbroic gneiss (Figure 5f; minimum $\varepsilon Hf = +8.40$). Zircon grains from the dyke are also highly radiogenic (Figure 5f; $\varepsilon Hf = +4.05$ to $+11.34$), but over half of the analyses are less radiogenic (Figure 5f; 10/19 grains with $\varepsilon Hf = +4.05$ to $+8.36$) than zircon in the gabbroic gneiss. Zircon from melferite samples have the most varied Hf isotopic character (Figure 5f; $\varepsilon Hf = -1.82$ to $+13.77$), where the least radiogenic grains all have apparent $^{206}Pb/^{238}U$ dates > 200 Ma (Table S1a).

4 | Discussion

4.1 | Zircon Coupled Dissolution–Precipitation Replacement Reactions Strongly Modifies Zircon Rare Earth Element Chemistry

Coupled dissolution–precipitation is a mineral replacement reaction process facilitated by fluids that reduces energy at the mineral-fluid interface (Putnis 2009; Ruiz-Agudo, Putnis, and Putnis 2014). Aqueous fluids or melts that dissolve minerals become locally saturated with components from the parent mineral and a new stable mineral crystallises on the parent mineral's surface (Putnis 2009). The replacement reaction migrates into the grain via a dynamic porosity network during repeated dissolution and precipitation (Beaudoin et al. 2018; Ruiz-Agudo, Putnis, and Putnis 2014), ultimately resulting in the complete replacement of the parent grain. Extended exposure to the fluid promotes healing of the porosity or crystallisation of other minerals to form epigenetic mineral inclusions (Spruzeniece et al. 2017). In our study, melt–zircon reactions during Types II and III melt–rock interaction replace parent zircon with new zircon that is more compositionally stable relative to the migrating melts.

The gabbro protolith to the Pembroke Granulite was emplaced at 131.3 ± 2.9 Ma (Hollis et al. 2003), and this is confirmed in this study by our zircon age in sample PV1232 (131.4 ± 1.2 Ma). Type I melt–rock interaction in the Pembroke Granulite occurred post-S1 and pre-D2; it involved diffuse porous melt flow through the gabbroic gneiss forming asymmetric coronae of pargasite-bearing symplectites around pyroxene grains (Figure 2a; Stuart, Piazolo, and Daczko 2016; Style 1 of Stuart, Piazolo, and Daczko 2018b). The relative modification of the protolith is low, and the simple zircon microstructure, geochronology and trace element chemistry documented for sample PV1232 indicates that this event did little to modify the primary zircon in the gabbroic gneiss.

Type II melt–rock interaction is associated with the melt-mediated reaction between the weakly hydrated gabbroic gneiss and D2 trondhjemitic dykes. This interaction forms distinctive garnet reaction zones that replace the two-pyroxene pargasite gneiss within < 80 mm wide high-P, melt-mediated, dehydration reaction haloes (Blattner 1976, 2005; Daczko, Clarke, and Klepeis 2001a; Clarke et al. 2005; Smith et al. 2015). Zircon separated from the garnet reaction zones (sample PV1234GRZ) exhibit microstructural and microchemical characteristics of coupled dissolution–precipitation replacement reactions (Putnis 2009): (i) pseudomorphism and dissolution leading to an irregularly shaped zircon with a pitted surface and embayed grain boundaries (white arrows, Figure 3c inset); (ii) porosity internal to the zircon (black arrows, Figure 3c inset); (iii) modified primary zircon growth zoning (compare the cathodoluminescence sector zoning in the gabbroic gneiss zircon, Figure 3a, with the blurred zoning in the garnet reaction zone zircon, Figure 3c); and (iv) compositionally distinct domains as shown by variable cathodoluminescence response (Figure 3c).

The garnet reaction zone zircon grains exhibit subtle rare earth element and variable Y depletion (Figure 5a,d) compared to the precursor gabbroic gneiss zircon. A common interpretation for this depletion involves garnet-zircon partitioning (e.g., Sláma, Košler, and Pedersen 2007). This interpretation can be argued more clearly for the depletion of heavy rare earth elements in zircon from the D2 dykes where this primary zircon and garnet both crystallised from a melt. However, the subtle rare earth element and variable Y depletion in the garnet reaction zone zircon grains (Figure 5a,d) aligns with chemical changes observed in experimental and natural instances of zircon coupled dissolution–precipitation replacement where garnet is not present (e.g., Soman et al. 2010). Depletion of trace elements occurs as trace element-enriched primary zircon with high structural strain is replaced by less soluble, trace element-poor zircon (reaction (1). The lost trace elements are most likely taken by the melt, as garnet is heavy rare earth element depleted in the garnet reaction zones (Schröter et al. 2004), suggesting that garnet did not noticeably sequester the minor release of heavy rare earth elements.

$$(Zr, Hf, Y, REE, Th, U)\,(Si, P)O4 + melt1 = (Zr, Hf)SiO4 + melt2 \quad \text{reaction 1}$$

The progression of Reaction (1) is more pronounced for Type III melt–rock interaction within our study. This Type III interaction is associated with highly localised melt migration, resulting in the formation of melferite high-strain zones (identified as Styles 3 and 4 in Stuart, Piazolo, and Daczko 2018b). These rocks are interpreted to have experienced a higher

time-integrated melt flux (Stuart, Piazolo, and Daczko 2018b), thereby amplifying the opportunities for melt–zircon reactions in comparison to Types I and II melt–rock interaction events. The migration of melt through melferite zones led to complete replacement and hydration of precursor gabbroic gneiss, dykes and garnet reaction zones, increasing the modes of amphibole, biotite and clinozoisite in the high-strain rocks (Stuart, Piazolo, and Daczko 2018b). Stuart et al. (2018a) suggest that high strain is achieved during melt-present deformation by grain boundary sliding accommodated by the movement of melt along grain boundaries. As such, the solid grains (including the zircon) experienced little to no crystal-plastic deformation. Therefore, chemical changes induced by crystal-plastic deformation of zircon (e.g., Piazolo, Austrheim, and Whitehouse 2012; Piazolo et al. 2016; Reddy et al. 2006; Timms, Kinny, and Reddy 2006; Timms et al. 2012) are likely of minor importance for this case study compared to the role played by coupled dissolution–precipitation.

Zircon extracted from the amphibolite melferite (sample PV1336) and hornblendite melferite (samples PV1514 and PV1520) display more conspicuous microstructural and microchemical characteristics associated with coupled dissolution–precipitation replacement reactions, as outlined by Putnis (2009), in contrast to zircon from the garnet reaction zones. Notably, the zircon from melferite samples exhibited pronounced embayed grain boundaries (Figure 3e,f), accompanied by well-developed dissolution pitting on the embayed surfaces (inset of Figure 3f). Both microstructures are interpreted to have formed during Type III melt–rock interaction. While the porosity density within the replaced zircon is variable (compare Figure 3e versus 3f), a substantial number of grains in the grain mounts revealed porosity in the exposed section (see the full grain mount images compiled in ImageMatrix, section 2.2.1). Moreover, the alteration of primary zircon growth zoning (Figure 3g) and variable cathodoluminescence response were more frequently observed in melferite zircon compared to those originating from the garnet reaction zones.

The chemical transformation of Group 1 melferite zircon is notably more pronounced following Type III melt–rock interaction, displaying intense depletion in heavy rare earth elements and Y (Figure 5c,d) and indicating a major change from the variable chemistry of the precursor zircon grains that originated from the precursor gabbroic gneiss, dykes and garnet reaction zones (Figure 5a–d). Group 1 melferite zircon also includes some xenocrysts up to c. 600 Ma (grain PV1520–17) that show the depleted chemical signal and indicates strong decoupling between the modification of the rare earth element patterns from variable modification of U–Pb ages. This extreme depletion may involve garnet-zircon partitioning in the melferite samples during Type III melt–rock interaction. Some of the heavy rare earth elements released from the zircon during coupled dissolution–precipitation replacement may viably have been sequestered into garnet rather than the melt2 of reaction (1).

Additionally, we observe two other distinct compositional groups within melferite zircon. A limited number of zircon grains either do not exhibit depletion in heavy rare earth elements (Group 2, depicted in green, Figure 5c,d) or demonstrate extreme depletion in light rare earth elements (Group 3, depicted in orange, Figure 5c,d), accompanied by very low U and Pb contents (Table S1a).

We interpret the Group 2 nondepleted zircon grains as xenocrysts transported by the upward-migrating melts moving through melferite high-strain zones based on their old spot dates. These grains likely experienced brief entrainment in the melts, limiting the coupled dissolution–precipitation process (e.g., see preservation of banded zoning and minor porosity in Figure 3d). While some of these zircon grains (e.g., Figure 3d) share similar ages with the studied rocks, most of them date back much further (> 400 Ma, Figures 3g and 5f) and were likely sourced from the Palaeozoic country rocks into which the Median Batholith was emplaced (Mortimer et al. 1999). The rare Group 3 zircon grains exhibiting extreme depletion in light rare earth elements are also considered xenocrysts in the migrating melts, given their distinct composition and high degree of modification. However, their history of melt–zircon reaction appears more complicated, and an alternative interpretation is that these represent extremely modified grains from the precursor rocks.

As noted by Altree-Williams et al. (2015), coupled dissolution–precipitation often involves a highly dynamic chemical system characterised by variable and changing fluid chemistry, temperature, pressure and reaction affinity. Determining the exact source of these highly modified Group 3 melferite zircon grains proves challenging, as their spot dates were highly unreliable, and they do not align with any documented zircon in the Fiordland arc lower crust. Therefore, these may represent zircon grains of variable original age (either extremely modified xenocrysts or grains from the precursor rocks) that are unique to the high time-integrated melt flux melferite zones due to their extreme modification.

4.2 | Mobility of Radiogenic Pb and Hf During Coupled Dissolution–Precipitation Replacement Reactions: Implications for Dating High-Grade Rocks

While the rare earth element patterns underwent significant modifications during the zircon coupled dissolution–precipitation replacement process (as detailed in Section 4.1), the mobility of other trace elements exhibited variability. The spectrum of apparent $^{206}Pb/^{238}U$ dates, spanning a range of about 20–25 million years (Figure 6d,e), in zircon extracted from both the garnet reaction zones and melferite high-strain zones indicates a nuanced redistribution of radiogenic Pb within the zircon crystals. Notably, there was minor Pb loss to the bulk melt. However, the zircon only had a brief period to accumulate radiogenic Pb following the emplacement of the gabbro pluton around 131 Ma (Hollis et al. 2003, this study). This period ended before the zircon underwent coupled dissolution–precipitation replacement during the melt rock interaction events. These interactions occurred within 5–10 million years, as indicated by garnet Sm-Nd geochronology, with Types II and III melt–rock interactions dated at 122.6 ± 2.0 and 126.0 ± 2.1 Ma, respectively (Stowell et al. 2010). Importantly, the age of the zircon was not completely reset during the coupled dissolution–precipitation replacement,

as indicated by the many spot dates spreading back to c. 131 Ma in the garnet reaction zone and melferite samples (Figure 6d,e). This creates a challenging scenario for dating the Type II and III melt–rock interaction events using zircon.

The close spatial proximity observed between the D2 trondhjemitic dykes and garnet reaction zones in the field as well as their documented direct causal relationship (Blattner 1976, 2005; Daczko, Clarke, and Klepeis 2001a; Daczko and Halpin 2009; Stowell et al. 2010) enables us to employ the weighted mean $^{206}Pb/^{238}U$ age of the dyke (123.5 ± 1.5 Ma) as a proxy for the age of the garnet reaction zones. However, only 5 out of 26 spot analyses of zircon from the garnet reaction zone fall within uncertainty of the dyke age itself, indicating that the coupled dissolution–precipitation only partially reset the age of the zircon (Figure 6d) and partially modified the rare earth element patterns (Figure 5a). Furthermore, six spot analyses from the zircon within the garnet reaction zone indicate dates up to approximately 10 million years younger than the dyke, suggesting the occurrence of subsequent Pb loss that affected these zircon grains. This observation underscores the susceptibility of zircon modified by coupled dissolution–precipitation replacement to subsequent Pb loss. We interpret that the porosity and inclusions formed during coupled dissolution–precipitation leave the replaced zircon in the garnet reaction zones much more accessible to later fluids and open to subsequent Pb-loss compared to zircon in the host gabbroic gneiss or dykes which are primary magmatic grains with higher structural integrity and resistance to Pb-loss. Moreover, it highlights the limited fidelity of zircon within the garnet reaction zones in accurately preserving the age or duration of the garnet granulite metamorphism.

The widespread distribution of zircon dates along concordia in metamorphic rocks has traditionally been employed to infer prolonged durations of metamorphism, ranging from tens to nearly one hundred million years (e.g., Clark et al. 2018; He et al. 2018; Korhonen et al. 2013; Laurent et al. 2018; Van Leeuwen et al. 2022). These extended timeframes pose challenges in sustaining elevated crustal temperatures. While many studies have used these date patterns in single samples as evidence for long-lived geological events, we caution that other scenarios are possible and recommend that high-resolution microstructural investigation of the zircon is needed to exclude the possibility of spurious spot date arrays caused by coupled dissolution–precipitation. In this study, we propose that it is highly improbable for the garnet reaction zones to have formed over tens of millions of years given the highly localised transformation to garnet granulite adjacent to dykes (e.g., Figure 6a). Instead, we argue that the array of nearly concordant spot dates may present misleading information regarding the actual duration of the garnet granulite-forming metamorphic event.

Similarly, our interpretation suggests that the migration of melt 'up' the melferite high-strain zones did not endure for tens of millions of years, leading to the spread of near-concordant spot dates observed in the melferite samples. We contend that these spot date spreads are artefacts arising from coupled dissolution–precipitation replacement reactions and do not accurately capture the true age or duration of the geological event. This interpretation is reinforced by the findings of melt–monazite reaction experiments (Varga et al. 2020) and melt–zircon reaction experiments (Asimus et al. 2024), which demonstrate that such spot date smears are not reliable indicators of the geological event's chronology.

The incomplete resetting of U–Pb isotopes in zircon arises from the dynamic process of Pb redistribution within the resultant zircon with or without loss to the bulk melt. As the parent zircon, enriched with trace elements, dissolves, elements displaying higher solubility and lesser compatibility within the newly forming zircon (such as Y, REE, P, U, Th and Pb) preferentially partition into the melt (Reaction (1). This elemental migration within the zircon grain occurs through a network of melt-filled porosity, moving from the reaction front to the broader bulk melt. However, these incompatible elements may experience temporary sequestration within transient porosity and micro-inclusions.

The efficiency of the exchange of these elements with the bulk melt hinges on several factors: (i) the interplay between compatibility of elements in the product zircon and the solubility of elements in the local melt; (ii) the diffusivity of these elements through the melt-filled porosity network, influenced by the chemical gradient between the reaction interface and the bulk melt reservoir; (iii) the connectivity of the melt network which is dynamic in space and time; and (iv) the precipitation of micro-inclusions within the product zircon and their stability throughout the ongoing coupled dissolution–precipitation process.

During zircon coupled dissolution–precipitation replacement, most trace elements analysed in this study undergo depletion (Figure 5 and Table S1c). However, the behaviour of Hf exhibits greater complexity during metamorphism as demonstrated in previous work where zircon Hf-isotopes have been shown to be largely decoupled from the U–Pb system (e.g., Gerdes and Zeh 2009) or modified along with the U–Pb system (e.g., Zheng et al. 2005). The zircon in gabbroic gneiss displays a relatively narrow compositional range (HfO2 = 1.05–1.20 wt.%), while the dyke zircon grains vary slightly on either side of this range (HfO2 = 0.93–1.30 wt.%). In the garnet reaction zone, zircon either overlaps with the chemical range or is depleted in Hf content (reaching as low as HfO2 = 0.97 wt.%) compared to the precursor gabbroic gneiss zircon. Notably, these lower Hf content zircon grains approach the range observed in the adjacent dyke, confirming chemical communication between the dyke melt and zircon coupled dissolution–precipitation replacement taking place in the garnet reaction zones. These changes to Hf content are possibly reflected in the Hf-isotopic ratios which show slightly more scatter in the garnet reaction zone zircon compared with the gabbroic gneiss zircon (Figure 5f) and align with changes to Hf-isotopes in metamorphic zircon elsewhere (e.g., Zheng et al. 2005).

In contrast, Group 1 melferite zircon generally exhibits an enrichment in Hf content (up to HfO2 = 1.78 wt.%), with a discernible weak correlation between heightened Hf content and younger apparent $^{206}Pb/^{238}U$ spot dates (Figure 5e). The xenocrystic nature interpreted for Groups 2 and 3 melferite zircon is supported by their highly variable Hf content (HfO2 = 0.80–1.28 wt.%), alongside the presence of some significantly older (> 400 Ma) grains than those from the

gabbroic gneiss (c. 131 Ma). Collectively, these compositional features of zircon highlight a generally weak coupling of trace element mobility during zircon coupled dissolution–precipitation replacement, consistent with other studies (e.g., Gerdes and Zeh 2009). While rare earth elements in most melferite zircon homogenised to a heavy rare earth element depleted composition, the redistribution and loss of Pb exhibit considerable variability. Simultaneously, the Hf content of zircon tends to decrease in the garnet reaction zones or increase in the melferite zones during melt–rock interaction. This variation in Hf behaviour is likely controlled by different melt compositions driving each melt–rock interaction event.

The nuanced chemistry observed in zircon can be ascribed to a confluence of factors. Firstly, heterogeneity may stem from the ablation of mixtures comprising both parent and product zircon, as proposed for monazite by Grand'Homme et al. (2016). Secondly, the alteration of zircon chemistry might transpire in either a relatively closed system (e.g., zircon coupled dissolution–precipitation replacement adjacent to a dyke) or a more intricate, evolving open system (exposed to various melt compositions flowing through the melferite zones, each melt having distinct capabilities to mobilise trace elements). Thirdly, the variable maturity of the product mineral could be linked to differing exposure durations and chemical interactions with the bulk melt, as elucidated by Borg et al. (2014), Spruzeniece et al. (2017), and Varga et al. (2020).

Moreover, chemical changes may extend beyond the coupled dissolution–precipitation process. Porosity generated during coupled dissolution–precipitation has the potential to serve as a facilitator for subsequent fluid ingress and/or diffusion of trace elements and Pb. It could also act as a site for the localization of deformation microstructures, subsequently functioning as fast diffusion pathways, as proposed by Timms et al. (2012).

The variations in the extent and characteristics of zircon modification, as highlighted in this study, serve as an independent indicator of the reactivity of the melt during interactions with rock. These findings can shed light on the pathways of melt migration, helping to differentiate between limited grain boundary diffusive flow resulting in minor zircon modification and widespread high flux melt migration leading to more substantial changes in zircon. To gain a more comprehensive understanding, further investigations should delve into the correlation between zircon microstructures and chemical diversity across various scales. Additionally, it is imperative to conduct further melt–zircon reaction experiments under crustal conditions using natural melts (e.g., Asimus et al. 2024). These experiments will provide crucial insights into the primary microchemical and microstructural signatures associated with the coupled dissolution–precipitation replacement of zircon.

5 | Conclusion

Our natural case study of zircon coupled dissolution–precipitation replacement reactions and the concurrent and subsequent modification of zircon chemistry shed light on complex geological processes that occur when variably reactive melts migrate through a rock. Melt-mediated coupled dissolution–precipitation serves as a transformative mechanism that replaces parent zircon with new, compositionally stable zircon where the chemical and isotopic make-up of the precursor zircon can be modified significantly.

The first Type I melt–rock interaction event experienced by the Pembroke Granulite was minor, and it had minimal impact on modification of the primary zircon grains, as evidenced by straightforward microstructures, geochronology and trace element chemistry. Type II melt–rock interaction involved the melt-mediated reaction between weakly hydrated gabbroic gneiss and D2 trondhjemitic dykes, dehydrating the host rock and forming garnet reaction zones. Notably, the garnet reaction zone zircon exhibited subtle rare earth element and Y depletion compared to the precursor gabbroic gneiss zircon. Type III melt–rock interaction, characterised by localised high time-integrated melt flux, yielded enhanced melt–zircon reactions. Zircon from these zones exhibits pronounced microstructural characteristics of coupled dissolution–precipitation replacement reactions, such as embayed grain boundaries, dissolution pitting and porosity. The chemical transformation of zircon during Type III melt–rock interaction is marked by intense depletion in heavy rare earth elements and Y.

The mobility of radiogenic Pb and Hf during zircon coupled dissolution–precipitation replacement revealed nuanced patterns. The apparent $^{206}Pb/^{238}U$ spot dates displayed variability, with some zircon grains experiencing minor Pb loss. The challenges in dating melt–rock interaction events using zircon highlight the complex nature of geological processes and the limitations of zircon as a reliable chronometer in some circumstances. Moreover, the widespread distribution of zircon spot dates along concordia, often interpreted to infer prolonged durations of metamorphism, is challenged by our study. Instead, we argue that these spot date arrays are artefacts of coupled dissolution–precipitation replacement reactions, emphasising the need for caution in interpreting zircon data in the context of age and duration of geological events.

Acknowledgements

This work builds on the data collected by Victoria Elliott for her Master of Research thesis at Macquarie University. We acknowledge Steven Craven, Manal Bebbington, Will Powell, David Adams, Rosanna Murphy, Sarah Gain, Nicole McGowan, Sean Murray, Yi-Jen Lai and Yoann Greau for facilitating laboratory analyses and Kim Jessop for helping collect the high-resolution BSE images used in this study. Rod McCallum kindly cut a large rock sample at the Northern Districts Lapidary Club. We thank Elena Belousova, John Gazi and Jeremy Asimus for providing constructive discussion about the microstructures formed during melt–zircon interaction and Cait Stuart and Uvana Meek for help in the field, providing key samples and for their foundational research on the melt–rock interaction styles of the Pembroke Granulite. This study was financially supported by Australian Research Council Discovery Project (DP200100482) and internally through the School of Natural Sciences, Macquarie University. We thank the reviewers (Nick Roberts and two anonymous reviewers) for their careful and constructive reviews and the editor (Clare Warren) for editorial handling.

Data Availability Statement

The data that support the findings of this study are available from the corresponding author upon reasonable request.

References

Allibone, A. H., R. Jongens, I. M. Turnbull, et al. 2009. "Plutonic Rocks of Western Fiordland, New Zealand: Field Relations, Geochemistry, Correlation, and Nomenclature." *New Zealand Journal of Geology and Geophysics* 52, no. 4: 379–415.

Altree-Williams, A., A. Pring, Y. Ngothai, and J. Brugger. 2015. "Textural and Compositional Complexities Resulting From Coupled Dissolution–Reprecipitation Reactions in Geomaterials." *Earth-Science Reviews* 150: 628–651.

Asimus, J. L., N. R. Daczko, J. A. Gazi, et al. 2024. "Experimental Replacement of Zircon by Melt-Mediated Coupled Dissolution-Precipitation Causes Dispersion in U-Pb Ages." *Journal of Metamorphic Geology* 1–17.

Beaudoin, N., A. Hamilton, D. Koehn, Z. K. Shipton, and U. Kelka. 2018. "Reaction-Induced Porosity Fingering: Replacement Dynamic and Porosity Evolution in the KBr-KCl System." *Geochimica et Cosmochimica Acta* 232: 163–180.

Belousova, E. A., W. L. Griffin, S. Y. O'Reilly, and N. L. Fisher. 2002. "Igneous Zircon: Trace Element Composition as an Indicator of Source Rock Type." *Contributions to Mineralogy and Petrology* 143: 602–622.

Belousova, E. A., Y. A. Kostitsyn, W. L. Griffin, G. C. Begg, S. Y. O'Reilly, and N. J. Pearson. 2010. "The Growth of the Continental Crust: Constraints From Zircon Hf-Isotope Data." *Lithos* 119, no. 3–4: 457–466.

Blattner, P. 1976. "Replacement of Hornblende by Garnet in Granulite Facies Assemblages Near Milford Sound, New Zealand." *Contributions to Mineralogy and Petrology* 55, no. 2: 181–190.

Blattner, P. 2005. "Transport of Low-aH2O Dehydration Products to Melt Sites Via Reaction-Zone Networks, Milford Sound, New Zealand." *Journal of Metamorphic Geology* 23, no. 7: 569–578.

Bogdanova, S. V., E. Belousova, B. De Waele, et al. 2021. "Palaeoproterozoic Reworking of Early Archaean Lithospheric Blocks: Rocks and Zircon Records From Charnockitoids in Volgo-Uralia." *Precambrian Research* 360: 106224.

Borg, S., W. Liu, M. Pearce, J. Cleverley, and C. MacRae. 2014. "Complex Mineral Zoning Patterns Caused by Ultra-Local Equilibrium at Reaction Interfaces." *Geology* 42, no. 5: 415–418.

Cherniak, D., and E. Watson. 2007. "Ti Diffusion in Zircon." *Chemical Geology* 242, no. 3–4: 470–483.

Cherniak, D. J., and E. B. Watson. 2003. "Diffusion in Zircon." *Reviews in Mineralogy and Geochemistry* 53, no. 1: 113–143.

Cherniak, D. J., E. B. Watson, M. Grove, and T. M. Harrison. 2004. "Pb Diffusion in Monazite: A Combined RBS/SIMS Study." *Geochimica et Cosmochimica Acta* 68, no. 4: 829–840.

Clark, C., R. J. Taylor, A. R. Kylander-Clark, and B. R. Hacker. 2018. "Prolonged (> 100 Ma) Ultrahigh Temperature Metamorphism in the Napier Complex, East Antarctica: A Petrochronological Investigation of Earth's Hottest Crust." *Journal of Metamorphic Geology* 36, no. 9: 1117–1139.

Clarke, G. L., N. R. Daczko, K. A. Klepeis, and T. Rushmer. 2005. "Roles for Fluid and/or Melt Advection in Forming High-P Mafic Migmatites, Fiordland, New Zealand." *Journal of Metamorphic Geology* 23, no. 7: 557–567.

Clarke, G. L., K. A. Klepeis, and N. R. Daczko. 2000. "Cretaceous High-P Granulites at Milford Sound, New Zealand: Metamorphic History and Emplacement in a Convergent Margin Setting." *Journal of Metamorphic Geology* 18, no. 4: 359–374.

Condie, K. C. 2018. "A Planet in Transition: The Onset of Plate Tectonics on Earth Between 3 and 2 Ga?" *Geoscience Frontiers* 9, no. 1: 51–60.

Condit, C. B., K. H. Mahan, K. C. Curtis, and A. Möller. 2018. "Dating Metasomatism: Monazite and Zircon Growth During Amphibolite Facies Albitization." *Minerals* 8, no. 5: 187.

Daczko, N. R., G. L. Clarke, and K. A. Klepeis. 2001a. "Transformation of Two-Pyroxene Hornblende Granulite to Garnet Granulite Involving Simultaneous Melting and Fracturing of the Lower Crust, Fiordland, New Zealand." *Journal of Metamorphic Geology* 19, no. 5: 549–562.

Daczko, N. R., G. L. Clarke, and K. A. Klepeis. 2002. "Kyanite-Paragonite-Bearing Assemblages, Northern Fiordland, New Zealand: Rapid Cooling of the Lower Crustal Root to a Cretaceous Magmatic Arc." *Journal of Metamorphic Geology* 20, no. 9: 887–902.

Daczko, N. R., and J. A. Halpin. 2009. "Evidence for Melt Migration Enhancing Recrystallization of Metastable Assemblages in Mafic Lower Crust, Fiordland, New Zealand." *Journal of Metamorphic Geology* 27, no. 2: 167–185.

Daczko, N. R., K. A. Klepeis, and G. L. Clarke. 2001b. "Evidence of Early Cretaceous Collisional-Style Orogenesis in Northern Fiordland, New Zealand and Its Effects on the Evolution of the Lower Crust." *Journal of Structural Geology* 23, no. 4: 693–713.

Daczko, N. R., and S. Piazolo. 2022. "Recognition of Melferite – A Rock Formed in syn-Deformational High-Strain Melt-Transfer Zones Through sub-Solidus Rocks: A Review and Synthesis of Microstructural Criteria." *Recognition of Melferite–A Rock Formed in Syn-Deformational High-Strain Melt-Transfer Zones Through Sub-Solidus Rocks: A Review and Synthesis of Microstructural Criteria. Lithos* 430-431: 106850.

Daczko, N. R., S. Piazolo, U. Meek, C. A. Stuart, and V. Elliott. 2016. "Hornblendite Delineates Zones of Mass Transfer Through the Lower Crust." *Scientific Reports* 6, no. 1: 31369.

Engi, M. 2017. "Petrochronology Based on REE-Minerals: Monazite, Allanite, Xenotime, Apatite." *Reviews in Mineralogy and Geochemistry* 83, no. 1: 365–418.

Exertier, F., A. La Fontaine, C. Corcoran, et al. 2018. "Atom Probe Tomography Analysis of the Reference Zircon GJ-1: An Interlaboratory Study." *Chemical Geology* 495: 27–35.

Flowers, R. M., A. K. Schmitt, and M. Grove. 2010. "Decoupling of U–Pb Dates From Chemical and Crystallographic Domains in Granulite Facies Zircon." *Chemical Geology* 270, no. 1–4: 20–30.

Fougerouse, D., T. Geisler, S. M. Reddy, et al. 2024. "Melt-Mediated Re-Equilibration of Zircon Produced During Meltdown of the Chernobyl Reactor." *American Mineralogist* 109, no. 1: 8–14.

Gain, S. E., Y. Gréau, H. Henry, et al. 2019. "Mud Tank Zircon: Long-Term Evaluation of a Reference Material for U-Pb Dating, Hf-Isotope Analysis and Trace Element Analysis." *Geostandards and Geoanalytical Research* 43, no. 3: 339–354.

Geisler, T., U. Schaltegger, and F. Tomaschek. 2007. "Re-Equilibration of Zircon in Aqueous Fluids and Melts." *Elements* 3, no. 1: 43–50.

Gerdes, A., and A. Zeh. 2009. "Zircon Formation Versus Zircon Alteration—New Insights From Combined U–Pb and Lu–Hf In-Situ LA-ICP-MS Analyses, and Consequences for the Interpretation of Archean Zircon From the Central Zone of the Limpopo Belt." *Chemical Geology* 261, no. 3–4: 230–243.

Grand'Homme, A., E. Janots, A. M. Seydoux-Guillaume, D. Guillaume, V. Bosse, and V. Magnin. 2016. "Partial Resetting of the U-Th-Pb Systems in Experimentally Altered Monazite: Nanoscale Evidence of Incomplete Replacement." *Geology* 44, no. 6: 431–434.

Griffin, W. L., E. A. Belousova, S. R. Shee, N. J. Pearson, and S. Y. O'reilly. 2004. "Archean Crustal Evolution in the Northern Yilgarn Craton: U–Pb and Hf-Isotope Evidence From Detrital Zircons." *Precambrian Research* 131, no. 3–4: 231–282.

Halpin, J. A., N. R. Daczko, N. G. Direen, J. A. Mulder, R. C. Murphy, and T. Ishihara. 2020. "Provenance of Rifted Continental Crust at the Nexus of East Gondwana Breakup." *Lithos* 354: 105363.

Halpin, J. A., N. R. Daczko, L. A. Milan, and G. L. Clarke. 2012. "Decoding Near-Concordant U–Pb Zircon Ages Spanning Several Hundred Million

Years: Recrystallisation, Metamictisation or Diffusion?" *Contributions to Mineralogy and Petrology* 163: 67–85.

He, X. F., M. Hand, M. Santosh, D. E. Kelsey, L. J. Morrissey, and T. Tsunogae. 2018. "Long-Lived Metamorphic P–T–T Evolution of the Highland Complex, Sri Lanka: Insights From Mafic Granulites." *Precambrian Research* 316: 227–243.

Hollis, J. A., G. L. Clarke, K. A. Klepeis, N. R. Daczko, and T. R. Ireland. 2003. "Geochronology and Geochemistry of High-Pressure Granulites of the Arthur River Complex, Fiordland, New Zealand: Cretaceous Magmatism and Metamorphism on the Palaeo-Pacific Margin." *Journal of Metamorphic Geology* 21, no. 3: 299–313.

Horstwood, M. S., J. Košler, G. Gehrels, et al. 2016. "Community-Derived Standards for LA-ICP-MS U-(Th-) Pb Geochronology–Uncertainty Propagation, Age Interpretation and Data Reporting." *Geostandards and Geoanalytical Research* 40, no. 3: 311–332.

Jackson, S. E., N. J. Pearson, W. L. Griffin, and E. A. Belousova. 2004. "The Application of Laser Ablation-Inductively Coupled Plasma-Mass Spectrometry to In Situ U–Pb Zircon Geochronology." *Chemical Geology* 211, no. 1–2: 47–69.

Jochum, K. P., B. Stoll, K. Herwig, and M. Willbold. 2007. "Validation of LA-ICP-MS Trace Element Analysis of Geological Glasses Using a New Solid-State 193 nm Nd: YAG Laser and Matrix-Matched Calibration." *Journal of Analytical Atomic Spectrometry* 22, no. 2: 112–121.

Kelly, C. J., D. A. Schneider, S. E. Jackson, T. Kalbfleisch, and C. R. McFarlane. 2017. "Insights Into Low-To Moderate-Temperature Recrystallization of Zircon: Unpolished Crystal Depth Profile Techniques and Geochemical Mapping." *Chemical Geology* 449: 82–98.

Kelsey, D. E., C. Clark, and M. Hand. 2008. "Thermobarometric Modelling of Zircon and Monazite Growth in Melt-Bearing Systems: Examples Using Model Metapelitic and Metapsammitic Granulites." *Journal of Metamorphic Geology* 26, no. 2: 199–212.

Kohn, M. J., M. S. Wieland, C. D. Parkinson, and B. N. Upreti. 2005. "Five Generations of Monazite in Langtang Gneisses: Implications for Chronology of the Himalayan Metamorphic Core." *Journal of Metamorphic Geology* 23, no. 5: 399–406.

Korhonen, F. J., C. Clark, M. Brown, S. Bhattacharya, and R. Taylor. 2013. "How Long-Lived Is Ultrahigh Temperature (UHT) Metamorphism? Constraints From Zircon and Monazite Geochronology in the Eastern Ghats Orogenic Belt, India." *Precambrian Research* 234: 322–350.

Kunz, B. E., D. Regis, and M. Engi. 2018. "Zircon Ages in Granulite Facies Rocks: Decoupling From Geochemistry Above 850°C?" *Contributions to Mineralogy and Petrology* 173: 1–21.

Kusiak, M. A., E. Kovaleva, R. Wirth, et al. 2019. "Lead Oxide Nanospheres in Seismically Deformed Zircon Grains." *Geochimica et Cosmochimica Acta* 262: 20–30.

Kusiak, M. A., M. J. Whitehouse, S. A. Wilde, A. A. Nemchin, and C. Clark. 2013. "Mobilization of Radiogenic Pb in Zircon Revealed by ion Imaging: Implications for Early Earth Geochronology." *Geology* 41, no. 3: 291–294.

Laurent, A. T., B. Bingen, S. Duchene, M. J. Whitehouse, A. M. Seydoux-Guillaume, and V. Bosse. 2018. "Decoding a Protracted Zircon Geochronological Record in Ultrahigh Temperature Granulite, and Persistence of Partial Melting in the Crust, Rogaland, Norway." *Contributions to Mineralogy and Petrology* 173: 1–25.

Martin, L. A., S. Duchêne, E. Deloule, and O. Vanderhaeghe. 2008. "Mobility of Trace Elements and Oxygen in Zircon During Metamorphism: Consequences for Geochemical Tracing." *Earth and Planetary Science Letters* 267, no. 1–2: 161–174.

Meek, U., S. Piazolo, and N. R. Daczko. 2019. "The Field and Microstructural Signatures of Deformation-Assisted Melt Transfer: Insights From Magmatic Arc Lower Crust, New Zealand." *Journal of Metamorphic Geology* 37, no. 6: 795–821.

Mezger, K., and E. J. Krogstad. 1997. "Interpretation of Discordant U-Pb Zircon Ages: An Evaluation." *Journal of Metamorphic Geology* 15, no. 1: 127–140.

Milan, L. A., N. R. Daczko, and G. L. Clarke. 2017. "Cordillera Zealandia: A Mesozoic Arc Flare-Up on the Palaeo-Pacific Gondwana Margin." *Scientific Reports* 7, no. 1: 261.

Milan, L. A., N. R. Daczko, G. L. Clarke, and A. H. Allibone. 2016. "Complexity of In-Situ Zircon U–Pb–Hf Isotope Systematics During arc Magma Genesis at the Roots of a Cretaceous Arc, Fiordland, NEW Zealand." *Lithos* 264: 296–314.

Miller, J. S., J. E. Matzel, C. F. Miller, S. D. Burgess, and R. B. Miller. 2007. "Zircon Growth and Recycling During the Assembly of Large, Composite Arc Plutons." *Journal of Volcanology and Geothermal Research* 167, no. 1–4: 282–299.

Möller, A., P. J. O'brien, A. Kennedy, and A. Kröner. 2002. "Polyphase Zircon in Ultrahigh-Temperature Granulites (Rogaland, SW Norway): Constraints for Pb Diffusion in Zircon." *Journal of Metamorphic Geology* 20, no. 8: 727–740.

Mortimer, N., A. J. Tulloch, R. N. Spark, et al. 1999. "Overview of the Median Batholith, New Zealand: A new Interpretation of the Geology of the Median Tectonic Zone and Adjacent Rocks." *Journal of African Earth Sciences* 29, no. 1: 257–268.

Paces, J. B., and J. D. Miller Jr. 1993. "Precise U-Pb Ages of Duluth Complex and Related Mafic Intrusions, Northeastern Minnesota: Geochronological Insights to Physical, Petrogenetic, Paleomagnetic, and Tectonomagmatic Processes Associated With the 1.1 Ga Midcontinent Rift System." *Journal of Geophysical Research: Solid Earth* 98, no. B8: 13997–14013.

Paterson, B. A., W. E. Stephens, G. Rogers, I. S. Williams, R. W. Hinton, and D. A. Herd. 1992. "The Nature of Zircon Inheritance in Two Granite Plutons." *Earth and Environmental Science Transactions of the Royal Society of Edinburgh* 83, no. 1–2: 459–471.

Piazolo, S., H. Austrheim, and M. Whitehouse. 2012. "Brittle-Ductile Microfabrics in Naturally Deformed Zircon: Deformation Mechanisms and Consequences for U-Pb Dating." *American Mineralogist* 97, no. 10: 1544–1563.

Piazolo, S., A. La Fontaine, P. Trimby, et al. 2016. "Deformation-Induced Trace Element Redistribution in Zircon Revealed Using Atom Probe Tomography." *Nature Communications* 7, no. 1: 10490.

Poulaki, E. M., D. F. Stockli, M. E. Flansburg, et al. 2021. "Zircon U-Pb and Geochemical Signatures in High-Pressure, Low-Temperature Metamorphic Rocks as Recorders of Subduction Zone Processes, Sikinos and IOS Islands, Greece." *Chemical Geology* 582: 120447.

Prent, A. M., A. Beinlich, L. J. Morrissey, T. Raimondo, C. Clark, and A. Putnis. 2019. "Monazite as a Monitor for Melt-Rock Interaction During Cooling and Exhumation." *Journal of Metamorphic Geology* 37, no. 3: 415–438.

Putnis, A. 2009. "Mineral Replacement Reactions." *Reviews in Mineralogy and Geochemistry* 70, no. 1: 87–124.

Reddy, S. M., N. E. Timms, P. Trimby, P. D. Kinny, C. Buchan, and K. Blake. 2006. "Crystal-Plastic Deformation of Zircon: A Defect in the Assumption of Chemical Robustness." *Geology* 34, no. 4: 257–260.

Reddy, S. M., N. E. Timms, W. Pantleon, and P. Trimby. 2007. "Quantitative Characterization of Plastic Deformation of Zircon and Geological Implications." *Contributions to Mineralogy and Petrology* 153, no. 6: 625–645.

Rubatto, D. 2017. "Zircon: The Metamorphic Mineral." *Reviews in Mineralogy and Geochemistry* 83, no. 1: 261–295.

Rubatto, D., O. Muentener, A. Barnhoorn, and C. Gregory. 2008. "Dissolution-Reprecipitation of Zircon at Low-Temperature, High-Pressure Conditions (Lanzo Massif, Italy)." *American Mineralogist* 93, no. 10: 1519–1529.

Ruiz-Agudo, E., C. V. Putnis, and A. Putnis. 2014. "Coupled Dissolution and Precipitation at Mineral–Fluid Interfaces." *Chemical Geology* 383: 132–146.

Scherer, E., C. Munker, and K. Mezger. 2001. "Calibration of the Lutetium-Hafnium Clock." *Science* 293, no. 5530: 683–687.

Schröter, F. C., J. A. Stevenson, N. R. Daczko, G. L. Clarke, N. J. Pearson, and K. A. Klepeis. 2004. "Trace Element Partitioning During High-P Partial Melting and Melt-Rock Interaction; an Example From Northern Fiordland, New Zealand." *Journal of Metamorphic Geology* 22, no. 5: 443–457.

Seydoux-Guillaume, A. M., B. Bingen, J. L. Paquette, and V. Bosse. 2015. "Nanoscale Evidence for Uranium Mobility in Zircon and the Discordance of U–Pb Chronometers." *Earth and Planetary Science Letters* 409: 43–48.

Skrzypek, E., S. Sakata, and D. Sorger. 2020. "Alteration of Magmatic Monazite in Granitoids From the Ryoke Belt (SW Japan): Processes and Consequences." *American Mineralogist* 105, no. 4: 538–554.

Sláma, J., J. Košler, and R. B. Pedersen. 2007. "Behaviour of Zircon in High-Grade Metamorphic Rocks: Evidence From Hf Isotopes, Trace Elements and Textural Studies." *Contributions to Mineralogy and Petrology* 154: 335–356.

Smith, J. R., S. Piazolo, N. R. Daczko, and L. Evans. 2015. "The Effect of pre-Tectonic Reaction and Annealing Extent on Behaviour During Subsequent Deformation: Insights From Paired Shear Zones in the Lower Crust of Fiordland, new Zealand." *Journal of Metamorphic Geology* 33, no. 6: 557–577.

Soman, A., T. Geisler, F. Tomaschek, M. Grange, and J. Berndt. 2010. "Alteration of Crystalline Zircon Solid Solutions: A Case Study on Zircon From an Alkaline Pegmatite From Zomba–Malosa, Malawi." *Contributions to Mineralogy and Petrology* 160: 909–930.

Spier, C. A., C. F. Ferreira Filho, and N. Daczko. 2022. "Zircon U-Pb Isotopic and Geochemical Study of Metanorites From the Chromite-Mineralised Bacuri Mafic-Ultramafic Complex: Insights of a Paleoarchean Crust in the Amapá Block, Guyana Shield, Brazil." *Gondwana Research* 105: 262–289.

Spruzeniece, L., S. Piazolo, N. R. Daczko, M. R. Kilburn, and A. Putnis. 2017. "Symplectite Formation in the Presence of a Reactive Fluid: Insights From Hydrothermal Experiments." *Journal of Metamorphic Geology* 35, no. 3: 281–299.

Stowell, H., A. Tulloch, C. Zuluaga, and A. Koenig. 2010. "Timing and Duration of Garnet Granulite Metamorphism in Magmatic Arc Crust, Fiordland, New Zealand." *Chemical Geology* 273, no. 1–2: 91–110.

Stuart, C. A., N. R. Daczko, and S. Piazolo. 2017. "Local Partial Melting of the Lower Crust Triggered by Hydration Through Melt–Rock Interaction: An Example From Fiordland, New Zealand." *Journal of Metamorphic Geology* 35, no. 2: 213–230.

Stuart, C. A., U. Meek, N. R. Daczko, S. Piazolo, and J. X. Huang. 2018a. "Chemical Signatures of Melt–Rock Interaction in the Root of a Magmatic Arc." *Journal of Petrology* 59, no. 2: 321–340.

Stuart, C. A., S. Piazolo, and N. R. Daczko. 2016. "Mass Transfer in the Lower Crust: Evidence for Incipient Melt Assisted Flow Along Grain Boundaries in the Deep Arc Granulites of F Iordland, New Z Ealand." *Geochemistry, Geophysics, Geosystems* 17, no. 9: 3733–3753.

Stuart, C. A., S. Piazolo, and N. R. Daczko. 2018b. "The Recognition of Former Melt Flux Through High-Strain Zones." *Journal of Metamorphic Geology* 36, no. 8: 1049–1069.

Sun, S. S., and W. F. McDonough. 1989. "Chemical and Isotopic Systematics of Oceanic Basalts: Implications for Mantle Composition and Processes." *Geological Society, London, Special Publications* 42, no. 1: 313–345.

Taylor, R. J., C. L. Kirkland, and C. Clark. 2016. "Accessories After the Facts: Constraining the Timing, Duration and Conditions of High-Temperature Metamorphic Processes." *Lithos* 264: 239–257.

Tichomirowa, M., M. J. Whitehouse, and L. Nasdala. 2005. "Resorption, Growth, Solid State Recrystallisation, and Annealing of Granulite Facies Zircon—A Case Study From the Central Erzgebirge, Bohemian Massif." *Lithos* 82, no. 1–2: 25–50.

Timms, N. E., P. D. Kinny, and S. M. Reddy. 2006. "Enhanced Diffusion of Uranium and Thorium Linked to Crystal Plasticity in Zircon." *Geochemical Transactions* 7, no. 1: 1–16.

Timms, N. E., S. M. Reddy, J. D. F. Gerald, L. Green, and J. R. Muhling. 2012. "Inclusion-Localised Crystal-Plasticity, Dynamic Porosity, and Fast-Diffusion Pathway Generation in Zircon." *Journal of Structural Geology* 35: 78–89.

Tulloch, A. J., and D. L. Kimbrough. 2003. "Paired Plutonic Belts in Convergent Margins and the Development of High Sr/Y Magmatism: Peninsular Ranges Batholith of Baja-California and Median Batholith of New Zealand." *Geological Society of America Special Paper* 374: 275–295.

Van Leeuwen, A. T. D. V., L. J. Morrissey, T. Raimondo, and M. Hand. 2022. "Prolonged High Thermal Gradient Metamorphism in the Curnamona Province, South-Central Australia, During the Latter Stages of Nuna Assembly." *Precambrian Research* 378: 106775.

Varga, J., T. Raimondo, N. R. Daczko, and J. Adam. 2020. "Experimental Alteration of Monazite in Granitic Melt: Variable U–Th–Pb and REE Mobility During Melt-Mediated Coupled Dissolution-Precipitation." *Chemical Geology* 544: 119602.

Vavra, G., D. Gebauer, R. Schmid, and W. Compston. 1996. "Multiple Zircon Growth and Recrystallization During Polyphase Late Carboniferous to Triassic Metamorphism in Granulites of the Ivrea Zone (Southern Alps): An ion Microprobe (SHRIMP) Study." *Contributions to Mineralogy and Petrology* 122, no. 4: 337–358.

Vermeesch, P. 2018. "IsoplotR: A Free and Open Toolbox for Geochronology." *Geoscience Frontiers* 9, no. 5: 1479–1493.

Vonlanthen, P., J. D. F. Gerald, D. Rubatto, and J. Hermann. 2012. "Recrystallization Rims in Zircon (Valle d'Arbedo, Switzerland): An Integrated Cathodoluminescence, LA-ICP-MS, SHRIMP, and TEM Study." *American Mineralogist* 97, no. 2–3: 369–377.

Weinberg, R. F., L. C. Wolfram, O. Nebel, et al. 2020. "Decoupled U-Pb Date and Chemical Zonation of Monazite in Migmatites: The Case for Disturbance of Isotopic Systematics by Coupled Dissolution-Reprecipitation." *Geochimica et Cosmochimica Acta* 269: 398–412.

Whitehouse, M. J., G. R. Ravindra Kumar, and A. Rimša. 2014. "Behaviour of Radiogenic Pb in Zircon During Ultrahigh-Temperature Metamorphism: An Ion Imaging and Ion Tomography Case Study From the Kerala Khondalite Belt, Southern India." *Contributions to Mineralogy and Petrology* 168: 1–18.

Wu, F. Y., Y. H. Yang, L. W. Xie, J. H. Yang, and P. Xu. 2006. "Hf Isotopic Compositions of the Standard Zircons and Baddeleyites Used in U–Pb Geochronology." *Chemical Geology* 234, no. 1–2: 105–126.

Yakymchuk, C., and M. Brown. 2014. "Behaviour of Zircon and Monazite During Crustal Melting." *Journal of the Geological Society* 171, no. 4: 465–479.

Zheng, Y. F., Y. B. Wu, Z. F. Zhao, S. B. Zhang, P. Xu, and F. Y. Wu. 2005. "Metamorphic Effect on Zircon Lu–Hf and U–Pb Isotope Systems in Ultrahigh-Pressure Eclogite-Facies Metagranite and Metabasite." *Earth and Planetary Science Letters* 240, no. 2: 378–400.

Supporting Information

Additional supporting information can be found online in the Supporting Information section.